

1 Ship-based lidar evaluation of Southern Ocean clouds 2 in the storm-resolving general circulation model ICON, 3 and the ERA5 and MERRA-2 reanalyses

4 Peter Kuma^{1,2,3*}, Frida A.-M. Bender^{1,2}, Adrian J. McDonald³, Simon P.
5 Alexander^{4,5}, Greg M. McFarquhar^{6,7}, John J. Cassano^{8,9,10}, Graeme E.
6 Plank³, Sean Hartery^{3†}, Simon Parsons^{3‡}, Sally Garrett¹¹, and Alex J.
7 Schuddeboom³

8 ¹Department of Meteorology (MISU), Stockholm University, Stockholm, Sweden

9 ²Bolin Centre for Climate Research, Stockholm University, Stockholm, Sweden

10 ³School of Physical and Chemical Sciences, University of Canterbury, Christchurch, Aotearoa/New
Zealand

11 ⁴Australian Antarctic Division, Kingston, Tasmania, Australia

12 ⁵Australian Antarctic Program Partnership, Institute for Marine and Antarctic Studies, University of
13 Tasmania, Hobart, Tasmania, Australia

14 ⁶Cooperative Institute of Severe and High Impact Weather Research and Operations, University of
15 Oklahoma, Norman, OK, USA

16 ⁷School of Meteorology, University of Oklahoma, Norman, OK, USA

17 ⁸Cooperative Institute for Research in Environmental Sciences, University of Colorado, Boulder, CO, USA

18 ⁹National Snow and Ice Data Center, University of Colorado, Boulder, CO, USA

20 ¹⁰Department of Atmospheric and Oceanic Sciences, University of Colorado, Boulder, CO, USA

21 ¹¹New Zealand Defence Force, Wellington, Aotearoa/New Zealand

22 Key Points:

- 23 • Ground-based lidar evaluation of a km-scale global climate model and reanalysis reveals substantial cloud biases over the Southern Ocean.
- 24 • Fog or low cloud is underestimated in the reanalyses. In all models, a cloud peak at 500 m tends to be overestimated and too high.
- 25 • A “too few, too bright” problem of underestimated cloud fraction, compensated by overestimated cloud albedo, is present in the reanalyses.
- 26
- 27
- 28

*

[†]Current affiliation: Department of Physics & Atmospheric Science, Dalhousie University, Halifax, Canada

[‡]Current affiliation: New South Wales Department of Planning and Environment, Sydney, New South Wales, Australia

Corresponding author: Peter Kuma, peter@peterkuma.net

29 **Abstract**

30 Global storm-resolving models (GSRMs) are the upcoming global climate models. One
 31 of them is a 5-km Icosahedral Nonhydrostatic Weather and Climate Model (ICON). Its
 32 high resolution means that parameterizations of convection and clouds, including subgrid-
 33 scale clouds, are omitted, relying on explicit simulation but still utilizing microphysics
 34 and turbulence parameterizations. Standard-resolution (10–100 km) models, which use
 35 convection and cloud parameterizations, have substantial cloud biases over the South-
 36 ern Ocean (SO), adversely affecting radiation and sea surface temperature. The SO is
 37 dominated by low clouds, which cannot be observed accurately from space due to over-
 38 lapping clouds, attenuation, and ground clutter. We evaluated SO clouds in ICON and
 39 the ERA5 and MERRA-2 reanalyses using about 2400 days of lidar observations and 2300
 40 radiosonde profiles from 31 voyages and Macquarie Island station during 2010–2021, com-
 41 pared with the models using a ground-based lidar simulator. We found that ICON and
 42 the reanalyses underestimate the total cloud fraction by about 10 and 20%, respectively.
 43 ICON and ERA5 overestimate the cloud occurrence peak at about 500 m, potentially
 44 explained by their lifting condensation levels being too high. The reanalyses strongly un-
 45 derestimate fog or near-surface clouds, and MERRA-2 underestimates cloud occurrence
 46 at almost all heights. Outgoing shortwave radiation is overestimated in the reanalyses,
 47 implying a “too few, too bright” cloud problem. Thermodynamic conditions are rela-
 48 tively well represented, but ICON is less stable than observations, and MERRA-2 is too
 49 humid. SO cloud biases are a substantial issue in the GSRM, but it matches the obser-
 50 vations better than the lower-resolution reanalyses.

51 **Plain Language Summary**

52 Global storm-resolving models are climate models with km-scale horizontal reso-
 53 lution, which are currently in development. Reanalyses are the best estimates of past
 54 meteorological conditions based on an underlying global model and observations. We eval-
 55 uated clouds and thermodynamic profiles over the Southern Ocean in one such model,
 56 as well as two reanalyses, based on 2400 days of ship and station observations. Thanks
 57 to the high resolution, the model relies entirely on explicit simulation of clouds, instead
 58 of subgrid-scale parameterizations. For the evaluation, we used ceilometer and radiosonde
 59 observations and a lidar simulator, which enables a fair comparison with the model and
 60 reanalyses. We subsetted our results by cyclonic activity and stability. We found that
 61 the model and reanalyses underestimate a lidar-derived cloud fraction, and the reanal-
 62 yses do so more strongly. Fog or near-surface clouds are especially underestimated in the
 63 reanalyses. However, the model and one of the reanalyses also tend to overestimate the
 64 peak of cloud occurrence at 500 m above the ground, and it tends to be higher. This is
 65 linked to thermodynamic profiles, which show a higher lifting condensation level. South-
 66 ern Ocean biases are still an important problem in the model, but an improvement over
 67 the reanalyses is notable.

68 **1 Introduction**

69 Increasing climate model resolution is one way of improving the accuracy of the
 70 representation of the climate system in models (Mauritsen et al., 2022). It has been prac-
 71 ticed since the advent of climate modeling as more computational power, memory, and
 72 storage capacity become available. It is, however, often not as easy as changing the grid
 73 size because of the complex interplay between model dynamics and physics, which ne-
 74 cessitates adjusting and tuning all components together. Increasing resolution is, of course,
 75 limited by the available computational power and a trade-off with increasing parame-
 76 terization complexity, which is another way of improving model accuracy. Current com-
 77 putational availability and acceleration from general-purpose computing on graphics pro-
 78 cessing units (GPUs) has progressed to enable km-scale (also called k-scale) Earth sys-

tem models (ESMs) and coupled atmosphere–ocean general circulation models (AOGCMs) for research today and will become operational in the future. Therefore, it represents a natural advance in climate modeling. Global storm-resolving models (GSRMs) are emerging as a new front in the development of high-resolution global climate models, with horizontal grid resolutions of about 2–8 km (Satoh et al., 2019; Stevens et al., 2019). This resolution is enough to resolve mesoscale convective storms, but smaller-scale convective plumes and cloud structure remain unresolved. At an approximately 5-km scale, non-hydrostatic processes also become important (Weisman et al., 1997), and for this reason such models are generally non-hydrostatic. The terms global cloud-resolving models or global convection-permitting/-resolving models are also sometimes used interchangeably with GSRMs but imply that clouds or convection are resolved explicitly, which is not entirely true for GSRMs, as this would require an even higher horizontal resolution (Satoh et al., 2019). Representative of these efforts is the DYnamics of the Atmospheric general circulation Modeled On Non-hydrostatic Domains (DYAMOND) project (Stevens et al., 2019; DYAMOND author team, 2024), which is an intercomparison of nine global GSRMs over two 40-day time periods in summer (1 August–10 September 2016) and winter (20 January–1 March 2020). A new one-year GSRM intercomparison is currently proposed by Takasuka et al. (2024), with the hope of also evaluating the seasonal cycle and large-scale circulation. An alternative to using a computationally costly GSRM is to train an artificial neural network on GSRM output and use it for subgrid-scale clouds, as done with the GSRM ICON by Grundner et al. (2022) and Grundner (2023).

The nextGEMS project (nextGEMS authors team, 2024) focuses on the research and development of GSRMs at multiple modeling centers and universities in Europe. The project also develops GSRM versions of the Icosahedral Nonhydrostatic Weather and Climate Model (ICON; Hohenegger et al. (2023)), the Integrated Forecasting System [IFS; ECMWF (2023)], and their ocean components at eddy-resolving resolutions: ICON-O (Korn et al., 2022) coupled with ICON and Finite-Element/volumE Sea ice-Ocean Model [FESOM; Q. Wang et al. (2014)] and Nucleus for European modeling of the Ocean [NEMO; Madec and the NEMO System Team (2023)] coupled with IFS. The project has so far produced ICON and IFS simulations with three development versions called Cycle 1–3 and a pre-final version, with a final production version planned by the end of the project. nextGEMS is not the only project developing GSRMs; other GSRMs (or GSRM versions of climate models) currently in development include: Convection-Permitting Simulations With the E3SM Global Atmosphere Model [SCREAM; Caldwell et al. (2021)], Atmospheric Model [NICAM; Satoh et al. (2008)], Unified Model (UM), eXperimental System for High-resolution modeling for Earth-to-Local Domain [X-SHiELD; SHiELD authors team (2024)], Action de Recherche Petite Echelle Grande Echelle-NonHydrostatic version [ARPEGE-NH; Bubnová et al. (1995); Volodire et al. (2017)], Finite-Volume Dynamical Core on the Cubed Sphere [FV3, Lin (2004)], the National Aeronautics and Space Administration (NASA) Goddard Earth Observing System global atmospheric model version 5 [GEOS5; Putman and Suarez (2011)], Model for Prediction Across Scales [MPAS; Skamarock et al. (2012)], and System for Atmospheric Modeling [SAM; Kharoutdinov and Randall (2003)].

Multiple cloud properties have an effect on shortwave (SW) and longwave (LW) radiation. To first order, the total cloud fraction, cloud phase, and the liquid and ice water path are the most important cloud properties influencing SW and LW radiation. These properties are in turn influenced by the atmospheric thermodynamics, convection and circulation, and both the indirect and direct effects of aerosols. Second-order effects on SW and LW radiation are associated with the cloud droplet size distribution, ice crystal habit, cloud lifetime, and direct radiative interaction with aerosols. In the 6th phase of the Coupled Model Intercomparison Project [CMIP6; Eyring et al. (2016)], the cloud feedback has increased relative to CMIP5 (Zelinka et al., 2020), which is one of the main reasons for the higher climate sensitivity of CMIP6 models.

The Southern Ocean (SO) is known to be a problematic region for climate model biases (A. J. Schuddeboom & McDonald, 2021; Hyder et al., 2018; Cesana et al., 2022; Zhao et al., 2022) due to a lack of surface and in situ observations and being a lower priority region for numerical weather prediction (NWP) and climate model development because of its distance from populated areas. Nevertheless, radiation biases and changes over an area of its size have a substantial influence on the global climate (Rintoul, 2011), such as affecting the Earth radiation balance, ocean heat, and carbon uptake (Williams et al., 2023), and the SO is also an important part of the global ocean conveyor belt (C. Wang et al., 2014). In general, marine clouds have a disproportionate effect on top-of-atmosphere (TOA) SW radiation due to the relatively low albedo of the sea surface. The relative longitudinal symmetry of the SO means that model cloud biases tend to be similar across longitudes.

Here, we refer to the SO as ocean regions south of 40°S, low-latitude SO as 40–55°S and high-latitude SO as south of 55°S. The reason for this dividing latitude is to split the SO into about two equal zones, as well as the results by A. J. Schuddeboom and McDonald (2021) (Fig. 2b) which show a contrast in CMIP model radiation biases. A. Schuddeboom et al. (2019) (Fig. 2) and Kuma et al. (2020) (Fig. 3) also show contrasting radiation biases in the Hadley Centre Global Environmental Model, which is also supported by Cesana et al. (2022) which displays contrasting cloud biases due to the 0°C isotherm reaching the surface at 55°S. The findings of Niu et al. (2024), however, support a different dividing line of 62°S based on cloud condensation nuclei concentration.

SO radiation biases have been relatively large and systematic compared to the rest of the globe since at least CMIP3 (Trenberth & Fasullo, 2010), and the SO SW cloud radiative effect (CRE) bias is still positive in eight analyzed CMIP6 models analyzed by A. J. Schuddeboom and McDonald (2021) over the high-latitude SO, whereas over the low-latitude SO it tends to be more neutral or negative in some models. Too much absorbed SW radiation over the SO was also identified in the GSRM SCREAM (Caldwell et al., 2021). Compensating biases are possible, such as the “too few too bright” cloud bias, characterized by too small cloud fraction and too large cloud albedo (Wall et al., 2017; Kuma et al., 2020), previously described by Webb et al. (2001), Weare (2004), M. H. Zhang et al. (2005), Karlsson et al. (2008), Nam et al. (2012), Klein et al. (2013), and Bender et al. (2017) in other regions and models, which means that a model can maintain a reasonable SW radiation balance by reflecting too much SW radiation from clouds, but these cover too small an area. A study by Konsta et al. (2022) showed that this type of bias is still present in six analyzed CMIP6 models in tropical marine clouds, using the GCM-Oriented Cloud-Aerosol Lidar and Infrared Pathfinder Satellite Observation (CALIPSO) Cloud Product [CALIPSO-GOCCP; Chepfer et al. (2010)] and Polarization & Anisotropy of Reflectances for Atmospheric Sciences coupled with Observations from a Lidar [PARASOL; Lier and Bach (2008)] as a reference. They suggest improper simulation of subgrid-scale cloud heterogeneity as a cause. Compensating cloud biases in the Australian Community Climate and Earth System Simulator (ACCESS) – Atmosphere-only model version 2 (AM2) over the SO were analyzed by Fiddes et al. (2022) and Fiddes et al. (2024). Possner et al. (2022) showed that over the SO, the DYAMOND GSRM ICON underestimates low-level cloud fraction on the order of 30% and overestimates net downward TOA SW radiation by approximately 10 W m⁻² in the highest model resolution run (2.5 km). Zhao et al. (2022) reported a similar SW radiation bias in five analyzed CMIP6 models over the high-latitude SO and an underestimation of the total cloud fraction on the order of 10% over the entire 40–60°S SO. Recently, Ramadoss et al. (2024) analyzed 48 hours of km-scale ICON limited-area model NWP simulations over a SO region adjacent to Tasmania against the Clouds, Aerosols, Precipitation, Radiation, and atmospherIc Composition Over the southeRN oceaN (CAPRICORN) voyage cloud and precipitation observations (McFarquhar et al., 2021). They found the ICON cloud optical thickness was underestimated relative to Himawari-8 satellite observations but also identified large differences in cloud top phase.

In general, sea surface temperature (SST) biases in the SO can originate either in the atmosphere (Hyder et al., 2018), caused by too much shortwave heating of the surface, too little longwave cooling of the surface, or in the ocean circulation. Interactions of both are also possible, for example, SST affecting clouds and clouds affecting the surface radiation. Using the European Centre for Medium-Range Weather Forecasts (ECMWF) Reanalysis 5 (ERA5) as a reference, Q. Zhang et al. (2023) have shown that SST biases have improved in CMIP6 compared to CMIP5, with SST overall increasing in CMIP6. However, over the SO this resulted in an even higher positive bias, especially in the Atlantic Ocean (AO) sector of the SO, increasing by up to 1°C. Luo et al. (2023) identified that the SO SST bias in an ensemble of 18 CMIP6 models originates not from the surface heat and radiation fluxes (using reanalyses as a reference), but from a warm bias in the Northern Atlantic Deep Water.

The main aim of this study is to evaluate the GSRM version of ICON. ICON is developed and maintained jointly by Deutscher Wetterdienst, Max-Planck-Institute for Meteorology, Deutsches Klimarechenzentrum (DKRZ), Karlsruhe Institute of Technology, and the Center for Climate Systems Modeling. Previous studies have identified substantial large-scale biases in climate model clouds over the SO, affecting sea surface temperature and the Earth's albedo. Our aim is to quantify how well the GSRM ICON simulates clouds in this region, particularly in light of the fact that subgrid-scale clouds and convection are not parameterized in this model. This region is mostly dominated by boundary layer clouds generated by shallow convection, and these are problematic to observe by spaceborne lidars and radars, which are affected by attenuation by overlapping and thick clouds (Mace et al., 2009; Medeiros et al., 2010) and ground clutter (Marchand et al., 2008), respectively. Specifically, the radar on CloudSat and lidar on CALIPSO (neither of which are now operational) are affected by the above-mentioned issues, resulting in a strong underestimation of cloud occurrence below 2 km relative to ground-based lidar observations (McErlich et al., 2021). We hypothesize that this, in turn, can lead to systematic biases in low clouds in climate models, which are frequently evaluated against CloudSat–CALIPSO products. Reanalyses can also suffer from cloud biases, as these are usually parameterized in their atmospheric component and also in regions where input observations are sparse. This makes them a problematic reference for clouds over the SO, and any biases relative to a reanalysis should be interpreted with caution. Instead, we chose to use a large set of ship-based observations conducted with ceilometers and lidars on board the RV *Polarstern* and other voyages and stations as a reference for the model evaluation.

Altogether, we analyzed about 2400 days of data from 31 voyages and one sub-Antarctic station covering diverse longitudes and latitudes of the SO. To achieve a like-for-like comparison with the model, we used a ground-based lidar simulator called the Automatic Lidar and Ceilometer Framework [ALCF; Kuma et al. (2021)]. We contrasted the results with ERA5 (ECMWF, 2019) and the Modern-Era Retrospective analysis for Research and Applications, Version 2 [MERRA-2; Gelaro et al. (2017)].

2 Methods

2.1 Voyage and Station Data

Together, we analyzed data from 31 voyages of RV *Polarstern*, the resupply vessel (RSV) *Aurora Australis*, RV *Tangaroa*, RV *Nathaniel B. Palmer*, Her (now His) Majesty's New Zealand Ship (HMNZS) *Wellington* and one sub-Antarctic station (Macquarie Island) in the SO south of 40°S between 2010 and 2021. Fig. 1 shows a map of the campaigns, Table 1 lists the campaigns, and Table 2 lists references where available. Altogether, the analyzed dataset comprised 2421 days of data south of 40°S, but the availability of ceilometer data was slightly shorter due to gaps in measurements.

The campaigns contained ceilometer observations captured by the Vaisala CL51, CT25K, and the Lufft CHM 15k, described in detail below (Sections 2.2 and 2.3). A ceilometer is a low-power, near-infrared, vertically pointing lidar principally designed to measure cloud base, but they also measure the full vertical structure of clouds as long as the laser signal is not attenuated by thick clouds, which can be used to infer additional information such as a cloud mask and cloud occurrence by height. We note that during the MICRE campaign, the ceilometers Vaisala CT25K and CL51 were installed at the Macquarie Island station concurrently, but in our analysis we only used the CT25K data obtained from the Atmospheric Radiation Measurement (ARM) data archive.

Apart from lidar observations, radiosondes were launched on weather balloons at regular synoptic times on the RV *Polarstern*, MARCUS, NBP17024, TAN1702, and TAN1802 campaigns, measuring pressure, temperature, relative humidity, and the global navigation satellite system coordinates. Derived thermodynamic (virtual potential temperature, lifting condensation level, etc.) and dynamic physical quantities (wind speed and direction) for the measured vertical profiles were calculated with *rstool* (Kuma, 2024).

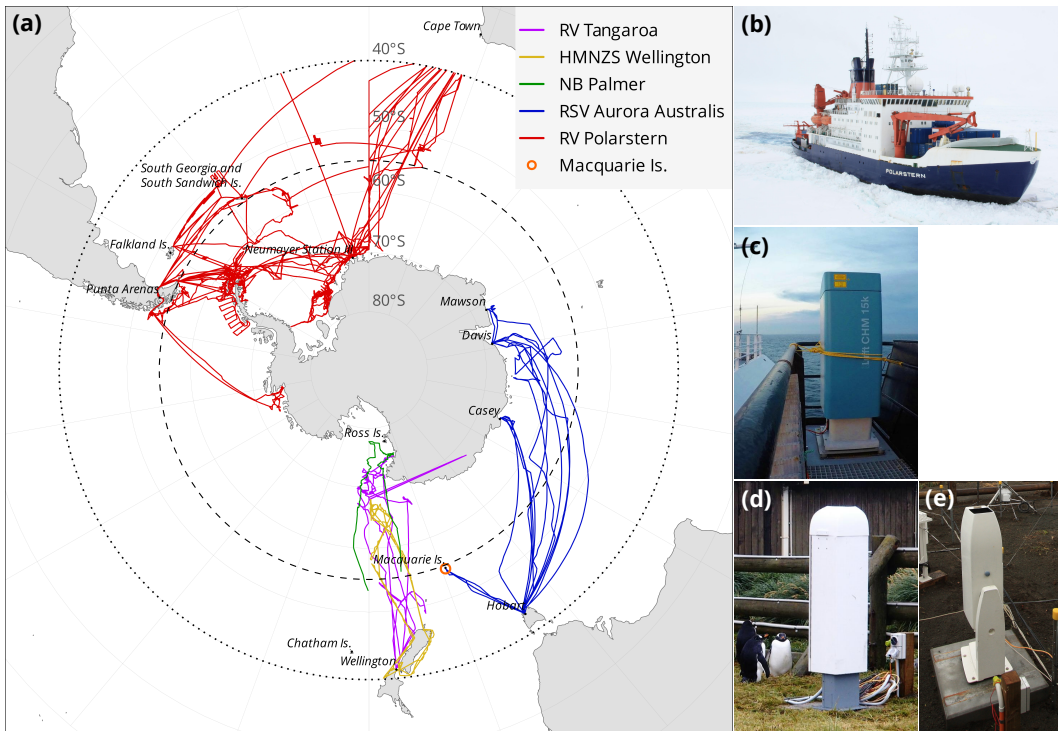


Figure 1. (a) A map showing the tracks of 31 voyages of RV *Polarstern*, RSV *Aurora Australis*, RV *Tangaroa*, RV *Nathaniel B. Palmer*, and HMNZS *Wellington* and one sub-Antarctic station (Macquarie Island) analyzed here. The tracks cover Antarctic sectors south of South America, the Atlantic Ocean, Africa, Australia, and New Zealand in the years 2010–2021 (inclusive). The dotted and dashed lines at 40°S and 55°S delineate the Southern Ocean area of our analysis and its partitioning into two subsets, respectively. A photo of (b) RV *Polarstern* (© Folke Mehrtens, Alfred-Wegener-Institut), (c) Lufft CHM 15k installed on RV *Tangaroa* (© Peter Kuma, University of Canterbury), (d) Vaisala CL51 (© Jeff Aquilina, Bureau of Meteorology), (e) Vaisala CT25K at Macquarie Island (© Simon P. Alexander, Australian Antarctic Division).

251 Surface meteorological quantities were measured continuously by an onboard automatic
252 weather station or individual instruments.

253 2.2 Vaisala CL51 and CT25K

254 The Vaisala CL51 and CT25K (photos in Fig. 1d, e) are ceilometers operating at
255 near-infrared wavelengths of 910 nm and 905 nm, respectively. The CL51 can also be
256 configured to emulate the Vaisala CL31. The maximum range is 15.4 km (CL51), 7.7 km
257 (CL31 emulation mode with 5 m vertical resolution), and 7.5 km (CT25K). The verti-
258 cal resolution is 10 m (5 m configurable) in CL51 and 30 m in CT25K observations. The
259 sampling (temporal) resolution is configurable, and in our datasets, it is approximately
260 6 s for CL51 on AA15-16, 16 s for CT25K on MARCUS and MICRE, 36 s for CL51 on
261 RV *Polarstern*, and about 2.37 s for CL51 with CL31 emulation on TAN1502. The wave-
262 lengths of 905 and 910 nm are both affected by water vapor absorption of about 20%
263 in the mid-latitudes (Wiegner & Gasteiger, 2015; Wiegner et al., 2019), with 910 nm af-
264 fected more strongly, but we do not expect this to be a significant issue as explained in
265 Kuma et al. (2021). The instrument data files containing raw uncalibrated backscatter
266 were first converted to Network Common Data Form (NetCDF) with cl2nc (<https://github.com/peterkuma/cl2nc>) and then processed with the ALCF (Section 2.4) to pro-
267 duce absolutely calibrated attenuated volume backscattering coefficient (AVBC), cloud
268 mask, cloud occurrence by height, and the total cloud fraction. Because the CT25K uses
269 a very similar wavelength to CL51, equivalent calculations as for CL51 were done assum-
270 ing a wavelength of 910 nm. The Vaisala CL51 and CT25K instruments were used on
271 most of the voyages and stations analyzed here. Fig. 2a shows an example of AVBC de-
272 rived from the CL51 instrument data.

274 2.3 Lufft CHM 15k

275 The Lufft CHM 15k (photo in Fig. 1c) ceilometer operates at a near-infrared wave-
276 length of 1064 nm. The maximum range is 15.4 km; the vertical resolution is 5 m in the
277 near range (up to 150 m) and 15 m above; the sampling (temporal) resolution is 2 s; and
278 the number of vertical levels is 1024. NetCDF files containing uncalibrated backscatter
279 produced by the instrument were processed with the ALCF (Section 2.4) to again pro-
280 duce AVBC, cloud mask, cloud occurrence by height, and the total cloud fraction. The
281 CHM 15k was used on four voyages (HMNZSW16, TAN1702, TAN1802, and NBP1704).

282 2.4 ALCF

283 The Automatic Lidar and Ceilometer Framework (ALCF) is a ground-based lidar
284 simulator and a tool for processing observed lidar data, supporting various instruments
285 and models (Kuma et al., 2021). It performs radiative transfer calculations to derive equiv-
286 alent lidar AVBC from an atmospheric model, which can then be compared with observed
287 AVBC. For this purpose, it takes the cloud fraction, liquid and ice mass mixing ratio,
288 temperature, and pressure model fields as an input and is run offline (on the model out-
289 put rather than inside the model code). The lidar simulator in the ALCF is based on
290 the instrument simulator Cloud Feedback Model Intercomparison Project (CFMIP) Ob-
291 servation Simulator Package (COSP) (Bodas-Salcedo et al., 2011). After AVBC is cal-
292 culated, a cloud mask, cloud occurrence by height, and the total cloud fraction are de-
293 termined. The ALCF has been used by several research teams for model and reanaly-
294 sis evaluation (Kuma et al., 2020; Kremser et al., 2021; Guyot et al., 2022; Pei et al., 2023;
295 Whitehead et al., 2023; McDonald, Kuma, et al., 2024).

296 Absolute calibration of the observed backscatter was performed by comparing the
297 measured clear-sky molecular backscatter statistically with simulated clear-sky molec-
298 ular backscatter. AVBC was resampled to 5 min temporal resolution and 50 m vertical
299 resolution to increase the signal-to-noise ratio while having enough resolution to detect

Table 1. An overview of the analyzed campaigns (voyages and stations). Start, end, and the number of days (UTC; inclusive) refer to the time period when the vessel was south of 40°S. Abbreviations: ceilometer (ceil.), Australia (AU), New Zealand (NZ), South America (SA), Atlantic Ocean (AO), and Africa (AF). The number of days is rounded to the nearest integer. CL51/31 indicates CL51 configured to emulate CL31. Missing days in the ceilometer data were HMNZSW16 (7 days): 24–27 November, 10 December, 16–17 December 2016; MARCUS (3 days): 8, 10 November, 10 December 2017; MICRE (9 days): 7–8, 29 June, 5, 16 July, 15 August, 17 October 2016, 11 February, 21 March 2017; TAN1502 (1 day): 24 January.

Name	Vessel or station	Ceil.	Region	Start	End	Days
AA15-16	RSV <i>Aurora Australis</i>	CL51	AU	2015-10-22	2016-02-22	124
HMNZSW16	HMNZS <i>Wellington</i>	CHM 15k	NZ	2016-11-23	2016-12-19	27
MARCUS	RSV <i>Aurora Australis</i>	CT25K	AU	2017-10-29	2018-03-26	149
MICRE	Macquarie Is. station	CT25K	AU/NZ	2016-04-03	2018-03-14	710
NBP1704	RV <i>Nathaniel B. Palmer</i>	CHM 15k	NZ	2017-04-14	2017-06-08	55
PS77/2	RV <i>Polarstern</i>	CL51	SA/AO/AF	2010-12-01	2011-02-04	65
PS77/3	RV <i>Polarstern</i>	CL51	SA/AO/AF	2011-02-07	2011-04-14	66
PS79/2	RV <i>Polarstern</i>	CL51	SA/AO/AF	2011-12-06	2012-01-02	27
PS79/3	RV <i>Polarstern</i>	CL51	SA/AO/AF	2012-01-10	2012-03-10	61
PS79/4	RV <i>Polarstern</i>	CL51	SA/AO/AF	2012-03-14	2012-04-08	26
PS81/2	RV <i>Polarstern</i>	CL51	SA/AO/AF	2012-12-02	2013-01-18	47
PS81/3	RV <i>Polarstern</i>	CL51	SA/AO/AF	2013-01-22	2013-03-17	55
PS81/4	RV <i>Polarstern</i>	CL51	SA/AO/AF	2013-03-18	2013-04-16	30
PS81/5	RV <i>Polarstern</i>	CL51	SA/AO/AF	2013-04-20	2013-05-23	33
PS81/6	RV <i>Polarstern</i>	CL51	SA/AO/AF	2013-06-10	2013-08-12	63
PS81/7	RV <i>Polarstern</i>	CL51	SA/AO/AF	2013-08-15	2013-10-14	60
PS81/8	RV <i>Polarstern</i>	CL51	SA/AO/AF	2013-11-12	2013-12-14	31
PS81/9	RV <i>Polarstern</i>	CL51	SA/AO/AF	2013-12-21	2014-03-02	71
PS89	RV <i>Polarstern</i>	CL51	SA/AO/AF	2014-12-05	2015-01-30	56
PS96	RV <i>Polarstern</i>	CL51	SA/AO/AF	2015-12-08	2016-02-14	68
PS97	RV <i>Polarstern</i>	CL51	SA/AO/AF	2016-02-15	2016-04-06	52
PS103	RV <i>Polarstern</i>	CL51	SA/AO/AF	2016-12-18	2017-02-02	46
PS104	RV <i>Polarstern</i>	CL51	SA/AO/AF	2017-02-08	2017-03-18	39
PS111	RV <i>Polarstern</i>	CL51	SA/AO/AF	2018-01-21	2018-03-14	52
PS112	RV <i>Polarstern</i>	CL51	SA/AO/AF	2018-03-18	2018-05-05	49
PS117	RV <i>Polarstern</i>	CL51	SA/AO/AF	2018-12-18	2019-02-07	51
PS118	RV <i>Polarstern</i>	CL51	SA/AO/AF	2019-02-18	2019-04-08	50
PS123	RV <i>Polarstern</i>	CL51	SA/AO/AF	2021-01-10	2021-01-31	21
PS124	RV <i>Polarstern</i>	CL51	SA/AO/AF	2021-02-03	2021-03-30	55
TAN1502	RV <i>Tangaroa</i>	CL51/31	NZ	2015-01-20	2015-03-12	51
TAN1702	RV <i>Tangaroa</i>	CHM 15k	NZ	2017-03-09	2017-03-31	23
TAN1802	RV <i>Tangaroa</i>	CHM 15k	NZ	2018-02-07	2018-03-20	41
Total					2421	

Table 2. Campaign publication references.

Name	References
AA15-16	Klekociuk et al. (2020)
MARCUS	McFarquhar et al. (2021); Xia and McFarquhar (2024); Niu et al. (2024)
MICRE	McFarquhar et al. (2021)
NBP1704	Ackley et al. (2020)
PS77/2	König-Langlo (2011e, 2011a, 2011c, 2014h); Fahrbach and Rohardt (2011)
PS77/3	König-Langlo (2011d, 2011b, 2012g, 2014i); Knust and Rohardt (2011)
PS79/2	König-Langlo (2012h, 2012d, 2012a, 2014j); Kattner and Rohardt (2012)
PS79/3	König-Langlo (2012i, 2012b, 2012e, 2014k); Wolf-Gladrow and Rohardt (2012)
PS79/4	König-Langlo (2012j, 2012c, 2012f, 2014l); Lucassen and Rohardt (2012)
PS81/2	König-Langlo (2013l, 2013a, 2013f, 2014a); Boebel and Rohardt (2013)
PS81/3	König-Langlo (2013m, 2013g, 2013b, 2014b); Gutt and Rohardt (2013)
PS81/4	König-Langlo (2013n, 2013c, 2013h, 2014c); Bohrmann and Rohardt (2013)
PS81/5	König-Langlo (2013o, 2013d, 2013i, 2014d); Jokat and Rohardt (2013)
PS81/6	König-Langlo (2013p, 2013e, 2013j, 2014e); Lemke and Rohardt (2013)
PS81/7	König-Langlo (2013q, 2013k, 2014f, 2016c); Meyer and Rohardt (2013)
PS81/8	König-Langlo (2013r, 2014g, 2014n, 2014p); Schlindwein and Rohardt (2014)
PS81/9	König-Langlo (2014r, 2014m, 2014o, 2014q); Knust and Rohardt (2014)
PS89	König-Langlo (2015a, 2015d, 2015b, 2015c); Boebel and Rohardt (2016)
PS96	König-Langlo (2016h, 2016a, 2016d, 2016f); Schröder and Rohardt (2017)
PS97	König-Langlo (2016i, 2016e, 2016b, 2016g); Lamy and Rohardt (2017)
PS103	König-Langlo (2017f, 2017d, 2017a, 2017c); Boebel and Rohardt (2018)
PS104	König-Langlo (2017e, 2017g, 2017b); Gohl and Rohardt (2018); Schmithüsen (2021g)
PS111	Schmithüsen (2019a, 2020a, 2021h, 2021a); Schröder and Rohardt (2018)
PS112	Schmithüsen (2019b, 2020b, 2021b, 2021i); Meyer and Rohardt (2018)
PS117	Schmithüsen (2019c, 2020c, 2021j, 2021c); Boebel and Rohardt (2019)
PS118	Schmithüsen (2019d, 2020d, 2021d, 2021k); Dorschel and Rohardt (2019)
PS123	Schmithüsen (2021m, 2021e, 2021l); Schmithüsen, Jens, and Wenzel (2021); Hoppmann, Tippenhauer, and Heitland (2023)
PS124	Schmithüsen (2021n, 2021f); Schmithüsen, Rohleider, et al. (2021); Hoppmann, Tippenhauer, and Hellmer (2023)
TAN1802	Kremser et al. (2020, 2021)

small-scale cloud variability. The noise standard deviation was calculated from AVBC at the highest range, where no clouds are expected. A cloud mask was calculated from AVBC using a fixed threshold of $2 \times 10^{-6} \text{ m}^{-1} \text{ sr}^{-1}$ after subtracting 5 standard deviations of range-scaled noise. Fig. 2b shows an example of simulated Vaisala CL51 backscatter from ERA5 data, corresponding to a day of measurements by the instrument on the PS81/3 voyage.

2.5 ICON

A coupled (atmosphere–ocean) GSRM version of the ICON model is in development as part of the nextGEMS project (Hohenegger et al., 2023). ICON is an exceptionally versatile model, allowing for simulations ranging from coarse-resolution ESM sim-

310 ulations, GSRM simulations, limited area model simulations, to large eddy simulations
 311 (LES), for both weather prediction and climate projections. ICON uses the atmospheric
 312 component ICON-A (Giorgetta et al., 2018), whose physics is derived from ECHAM6
 313 (Stevens et al., 2013), and the ocean component ICON-O (Korn et al., 2022). Earlier runs
 314 of the GSRM ICON from DYAMOND were evaluated by Mauritsen et al. (2022).

315 Here, we use a free-running (i.e., the weather situation in the model does not cor-
 316 respond to reality) coupled GSRM simulation made for the purpose of climate projec-
 317 tion. nextGEMS has so far produced four cycles of model runs. We used a Cycle 3 run
 318 *ngc3028* produced in 2023 (Koldunov et al., 2023; nextGEMS authors team, 2023) for
 319 a model time period of 20 January 2020 to 22 July 2025, of which we analyzed the pe-
 320 riod 2021–2024 (inclusive). The horizontal resolution of *ngc3028* is about 5 km. The model
 321 output is available on 90 vertical levels and 3-hourly instantaneous temporal resolution.

322 Unlike current general circulation models (GCMs), the storm-resolving version of
 323 ICON does not use convective and cloud parameterization but relies on explicit simu-
 324 lation of convection and clouds on the model grid. Subgrid-scale clouds are not resolved,
 325 and the grid cell cloud fraction is always either 0 or 100%. While this makes the code
 326 development simpler without having to rely on uncertain parameterizations, it can miss
 327 smaller-scale clouds below the grid resolution. Turbulence and cloud microphysics are
 328 still parameterized in this model, and aerosols are taken from a climatology. To account
 329 for the radiative effects of subgrid-scale clouds, a cloud inhomogeneity factor is introduced
 330 in the model, which scales down the cloud liquid water for radiative calculations. It ranges
 331 from 0.4 at lower tropospheric stability (LTS) of 0 K to 0.8 at 30 K. In addition, ver-

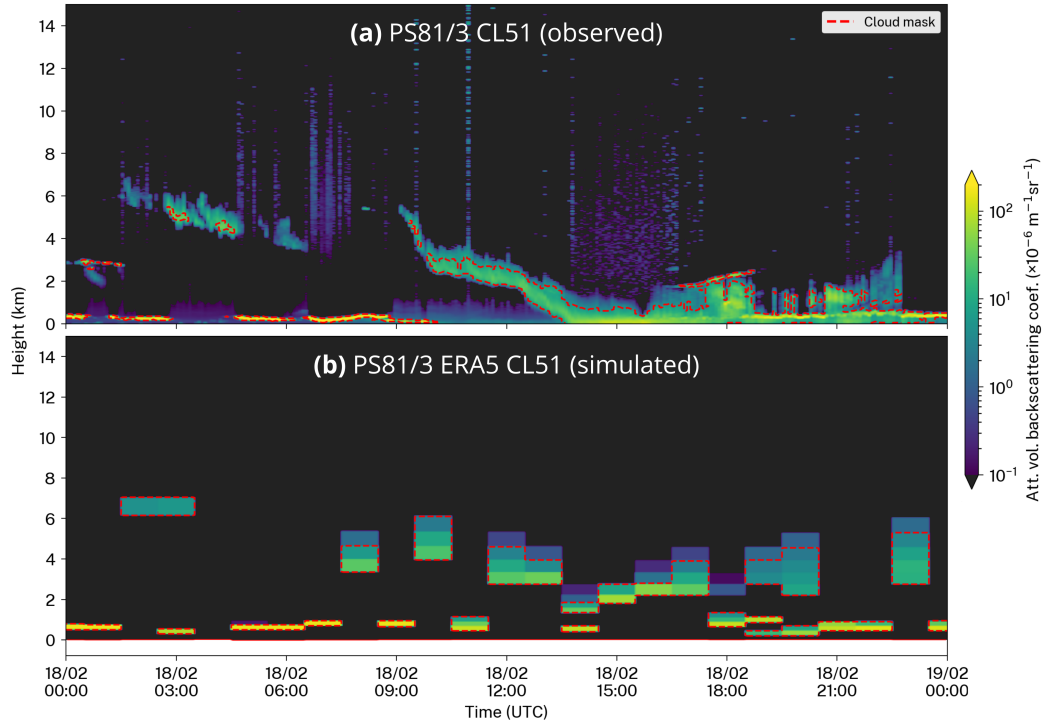


Figure 2. An example of the attenuated volume backscattering coefficient (AVBC) (a) mea-
 sured by the CL51 during 24 hours on the PS81/3 voyage and (b) an equivalent AVBC simu-
 lated with the ALCF from ERA5 data during the same time period. The red line identifies the
 cloud mask determined by the ALCF.

332 tical mixing is enhanced in unstable and humid lower-tropospheric conditions, which re-
 333 duces the amount of shallow clouds.

334 Because the analyzed ICON simulation was free-running (years 2021–2024, inclu-
 335 sive), weather and climate oscillations (such as the El Niño–Southern Oscillation) are
 336 not expected to be equivalent to reality at the same time and place. To compare with
 337 the observations collected during a different time period (years 2010–2021, inclusive), we
 338 compared the model output with observations at the same time of year and geograph-
 339 ical location, as determined for each data point, such as a lidar profile or a radiosonde
 340 launch. In the ALCF, this was done using the *override_year* option (https://alcf.peterkuma.net/documentation/cli/cmd_model.html). For radiosonde profiles, the same map-
 341 ping of time from was done. That is, when selecting an equivalent profile from the model,
 342 the time of the profile was changed so that the time relative to the start of the year was
 343 preserved, but the year was changed to one of the four years available in the model data.
 344 Thus, for every radiosonde launch, there were four equivalent model profiles. The geo-
 345 graphical location was kept the same. We discuss briefly the implications of comparing
 346 the observations with a free-running model in Section 4.

348 2.6 MERRA-2

349 The Modern-Era Retrospective analysis for Research and Applications, Version 2
 350 (MERRA-2) is a reanalysis produced by the Global Modeling and Assimilation Office
 351 at the NASA Goddard Space Flight Center (Gelaro et al., 2017). It uses version 5.12.4
 352 of the Goddard Earth Observing System (GEOS) atmospheric model (Rienecker et al.,
 353 2008; Molod et al., 2015). Non-convective clouds (condensation, autoconversion, and evap-
 354 oration) are parameterized using a prognostic scheme (Bacmeister et al., 2006), and sub-
 355 grid cloud fraction is determined using total water distribution and a critical relative hu-
 356 midity threshold. The reanalysis output analyzed here is available at a spatial resolu-
 357 tion of 0.5° of latitude and 0.625° of longitude, which is about 56 km in the North–South
 358 direction and 35 km in the East–West direction at 60°S. The number of vertical model
 359 levels is 72. Here, we use the following products: 1-hourly instantaneous 2D single-level
 360 diagnostics (M2I1NXASM) for 2-m temperature and humidity; 3-hourly instantaneous
 361 3D assimilated meteorological fields (M2I3NVASM) for cloud quantities, pressure, and
 362 temperature; 1-hourly average 2D surface flux diagnostics (M2T1NXFLX) for precip-
 363 itation; and 1-hourly average 2D radiation diagnostics (M2T1NXRAD) for radiation quan-
 364 tities (Bosilovich et al., 2016).

365 2.7 ERA5

366 ERA5 (ECMWF, 2019) is a reanalysis produced by the ECMWF. It is based on
 367 a numerical weather prediction model IFS version CY41R2. It uses the Tiedtke (1993)
 368 prognostic cloud scheme and Forbes and Ahlgrimm (2014) for mixed-phase clouds. The
 369 horizontal resolution is 0.25° in latitude and longitude, which is about 28 km in the North–
 370 South direction and 14 km in the East–West direction at 60°S. Internally, the model uses
 371 137 vertical levels. Here, we use output at 1-hourly instantaneous time intervals, except
 372 for radiation quantities, which are accumulations (from these we calculate daily means).
 373 Vertically resolved quantities are made available on 37 pressure levels.

374 2.8 CERES

375 TOA radiation quantities are taken from the CERES instruments onboard the Terra
 376 and Aqua satellites (Wielicki et al., 1996; Loeb et al., 2018). In our analysis, we used
 377 the adjusted all-sky SW and LW upwelling fluxes at TOA from the synoptic TOA and
 378 surface fluxes and clouds 1-degree daily edition 4A product (CER_SYN1deg-Day_Terra-
 379 Aqua-MODIS_Edition4A) (Doelling et al., 2013, 2016).

380 Radiation calculations presented in the results (Section 3) were completed such that
 381 they always represent daily means in order to be consistent with the CERES SYN1deg
 382 data. Therefore, every instantaneous profile in the simulated lidar data was assigned a
 383 daily mean radiation value corresponding to the day (in the Coordinated Universal Time;
 384 UTC). In turn, the average radiation during the entire voyage or station observation pe-
 385 riod was calculated as the average of the profile values. In the observed lidar data, the
 386 daily mean radiation value was taken from the spatially and temporally co-located CERES
 387 SYN1deg data for the day (in UTC). The voyage or station average was calculated in
 388 the same way.

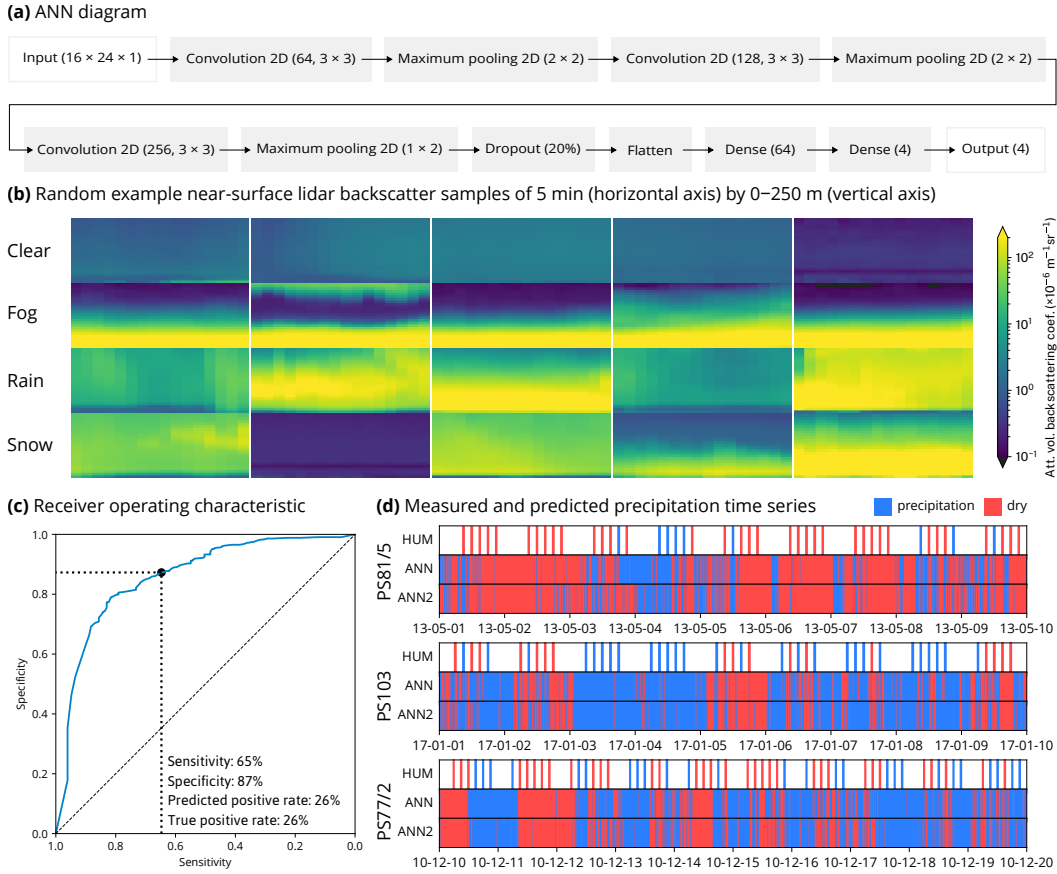


Figure 3. Artificial neural network (ANN) for prediction of precipitation in lidar backscatter. **(a)** Diagram showing the TensorFlow structure of the ANN, **(b)** randomly selected example samples of near-surface backscatter in four categories (clear, fog, rain, and snow), as determined by coincident manual weather observations, **(c)** receiver operating characteristic diagram of the ANN, **(d)** examples of 10-day time series of human-observed (“HUM”) and predicted precipitation based on an ANN trained on all voyages (“ANN”) and all voyages except for the shown voyage (“ANN2”) during three randomly selected voyages with the available data. Here, by “randomly selected,” we mean selected from the top of a permutation generated by a pseudo-random number generator to prevent authors’ bias in the selection.

489 2.9 Precipitation Identification Using Machine Learning

490 Precipitation can cause strong enough lidar backscattering to be recognized as clouds
 491 by the threshold-based cloud detection method used in the ALCF. This is undesirable
 492 if equivalent precipitation backscatter is not included in the simulated lidar profiles. It
 493 was not possible to include precipitation simulation in the ALCF due to the absence of
 494 required fields in the ICON model output and the reanalysis data (the liquid and ice pre-
 495 precipitation mass mixing ratios). The required radiation calculations for precipitation are
 496 also currently not implemented in the ALCF, even though this is a planned future ad-
 497 dition. In order to achieve a fair comparison of observations with model output, we ex-
 498 clude observed and simulated lidar profiles with precipitation, either manually or using
 499 an automated method. It is relatively difficult to distinguish precipitation backscatter
 500 from cloud backscatter in lidar observations, especially when only one wavelength chan-
 501 nel and no polarized channel are available. In models, the same can be accomplished rel-
 502 atively easily by excluding profiles exceeding a certain surface precipitation flux. In the
 503 observations, using precipitation flux measurements from rain gauges can be very un-
 504 reliable on ships due to ship movement, turbulence caused by nearby ship structures, and
 505 sea spray. Our analysis of rain gauge data from the RV *Tangaroa* showed large discrep-
 506 ancies between the rain gauge time series and human-performed synoptic observations,
 507 as well as large inconsistencies in the rain gauge time series. Human-performed obser-
 508 vations of precipitation presence or absence are expected to be reliable but only cover
 509 a limited set of times. Therefore, it was desirable to implement a method of detecting
 510 precipitation from observed backscatter profiles alone.

511 On the RV *Polarstern* voyages, regular manual synoptic observations were avail-
 512 able and included precipitation presence or absence and type. We used this dataset to
 513 train a convolutional artificial neural network (ANN) to recognize profiles with precipi-
 514 tation from lidar backscatter data (Fig. 3a), implemented in the TensorFlow ANN frame-
 515 work (Abadi et al., 2015). Samples of short time intervals (10 min) of near-surface li-
 516 dar backscatter (0–250 m) were classified as clear, rain, snow, and fog, using the synop-
 517 tic observations as a training dataset (Fig. 3b). From these, a binary, mutually exclu-
 518 sive classification of profiles as precipitating (rain or snow) or dry (clear or fog) was de-
 519 rived. For detecting model and reanalysis precipitation, we used a fixed threshold for sur-
 520 face precipitation flux of 0.1 mm h^{-1} (the ANN was not used).

521 The ANN achieved 65% sensitivity and 87% specificity when the true positive rate
 522 (26%) was made to match observations. The receiver operating characteristic curve is
 523 shown in Fig. 3c. We considered these rates satisfactory for the purpose of filtering pre-
 524 cipitation profiles. Fig. 3d shows examples of the predicted precipitation compared to
 525 human-performed observations. The main ANN ('ANN' in Fig. 3) was trained on all data,
 526 and ancillary ANNs ('ANN2' in Fig. 3) were trained with portions of voyage data ex-
 527 cluded to test the results for each voyage.

528 2.10 Partitioning by Cyclonic Activity and Stability

529 We partitioned our data into two mutually exclusive subsets by cyclonic activity.
 530 For this purpose, we used a cyclone tracking algorithm to identify extratropical and po-
 531 lar cyclones (ECs and PCs) over the SO in the reanalysis and ICON data. We used the
 532 open-source cyclone tracking package CyTRACK (Pérez-Alarcón et al., 2024). Gener-
 533 ally, what constitutes an EC is considered relatively arbitrary due to the very large vari-
 534 ability of ECs (Neu et al., 2013). The CyTRACK algorithm uses mean sea level pres-
 535 sure and wind speed thresholds as well as tracking across time steps to identify cyclone
 536 centers and radii in each time step. With this information, we could classify geographical
 537 areas as either cyclonic or non-cyclonic. Due to a relatively small total area covered
 538 by cyclones (as identified by the cyclone center and radius), we chose a circle of double
 539 the radius (relative to one identified by CyTRACK) centered at the cyclone center as

a cyclonic area for every time step and cyclone. All other areas were identified as non-cyclonic. For identifying cyclones in the observations and the reanalyses, ERA5 pressure and wind fields were used as the input to CyTRACK. This is justified by the fact that the large-scale pressure and wind fields in ERA5 are likely sufficiently close to reality. McErlich et al. (2023) have shown that wind is simulated well in ERA5 relative to the WindSat polarimetric microwave radiometer measurements (Meissner & Wentz, 2009). For identifying cyclones in ICON, its own pressure and wind fields were used as the input to CyTRACK, because the model is free-running, and thus the pressure and wind fields are different from reality. Subsetting by proximity to cyclones is a relatively crude measure because it does not take into account the different sectors of cyclones, which are commonly associated with different weather situations. However, this was a choice made for simplicity of the analysis, given the quantity of data.

In addition to the above, we partitioned our data into two mutually exclusive subsets based on LTS, which is derived as the difference between the potential temperature at 700 hPa and the surface. Based on a histogram of LTS in ERA5 and MERRA-2 calculated at all voyage tracks and stations (Fig. 4), we determined a statistically-based dividing threshold of 12 K for weak stability (< 12 K) and strong stability (≥ 12 K) conditions.

3 Results

3.1 Cyclonic Activity and Stability

Fig. 5a, b show the geographical distribution of the fraction of cyclonic days as determined by the cyclone tracking algorithm applied to the ERA5 reanalysis and ICON data (Section 2.10). As expected, the strongest cyclonic activity is in the high-latitude SO zone and is relatively zonally symmetric at all latitudes. The pattern matches reasonably well with Hoskins and Hodges (2005). While both reanalysis and the model agree within about 8% in most areas, ICON is prevailingly more cyclonic by about 4%. There are clear differences, particularly in the highest occurrence rate regions, such as around Cape Adare, which is up to 20% more cyclonic in ICON, and the Weddell and Bellingshausen Seas, where ICON is less cyclonic by up to 10%. These differences might, how-

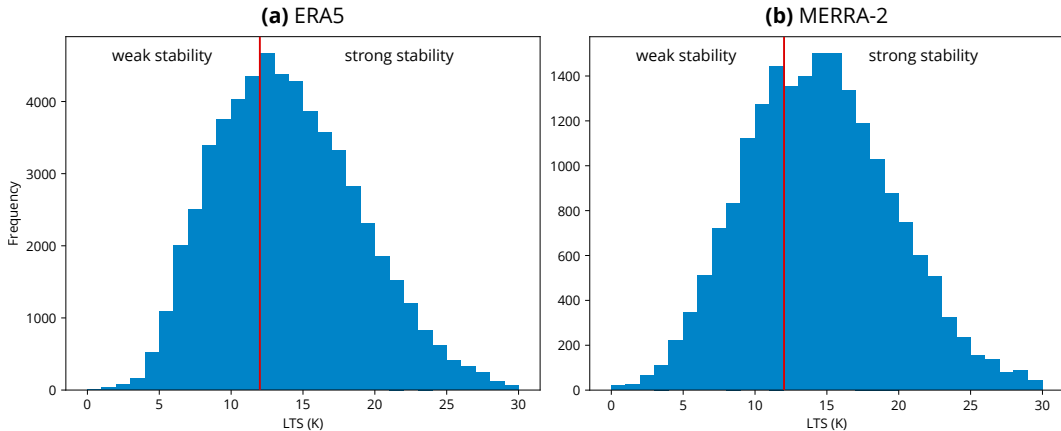


Figure 4. Lower tropospheric stability (LTS) distribution in (a) ERA5 and (b) MERRA-2 calculated for the 31 voyage tracks and one station from the highest instantaneous temporal resolution data available. Shown is also the chosen dividing threshold of 12 K for conditions of weak and strong stability.

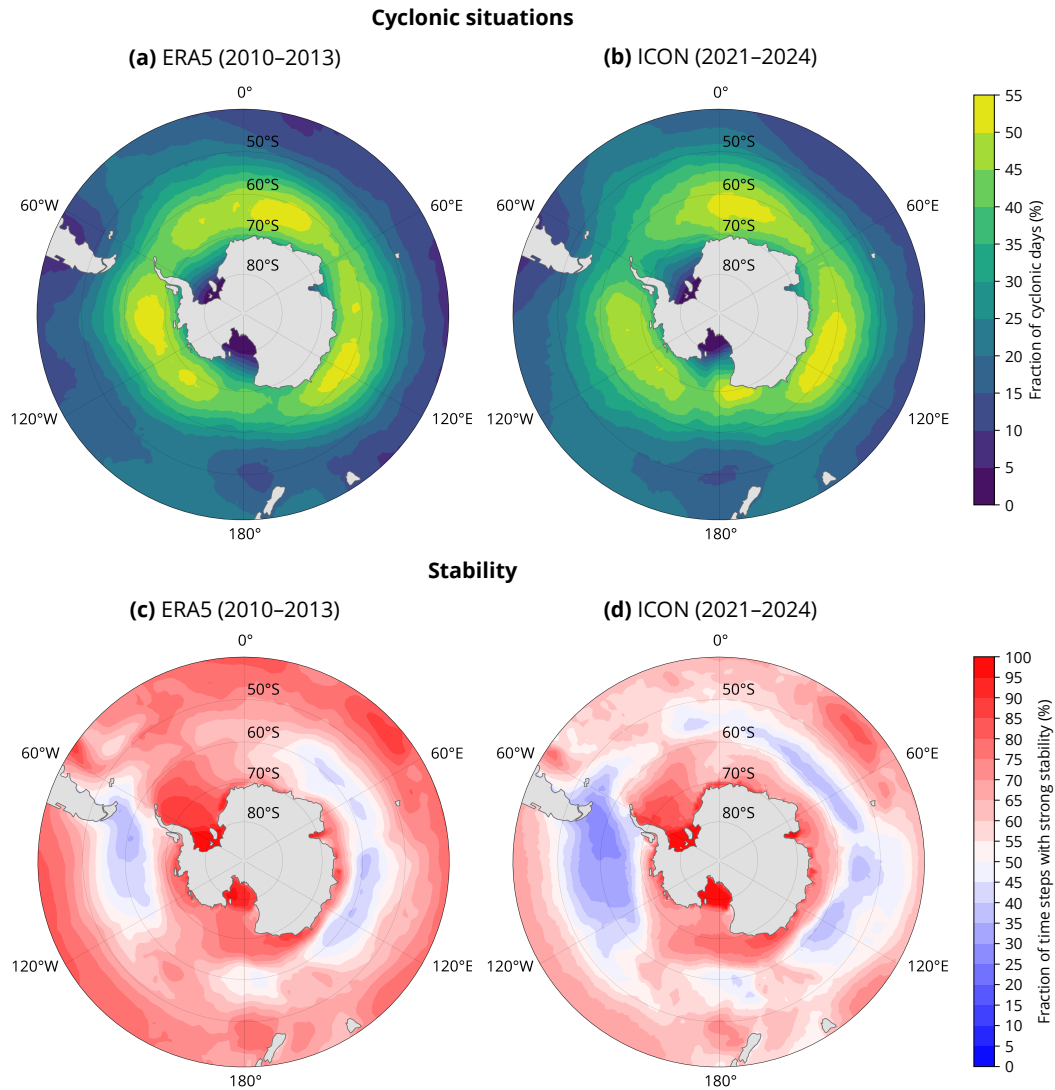


Figure 5. Geographical distribution of (a, b) cyclonic days and (b, d) strong stability ($LTS \geq 12$ K) time steps in (a, c) ERA5 in years 2010–2013 (inclusive) and (b, d) ICON in model years 2021–2023 (free running). Cyclonic days are expressed as a fraction of the number of days with cyclonic activity, defined as grid points located within a double radius of any cyclone on a given day (UTC), as identified by CyTRACK.

ever, stem from the relatively short time periods of comparison (4 years) and the fact that the model is free-running.

Fig. 5c, d show the geographical distribution of the conditions of weak and strong stability as determined by the LTS (Section 2.10). Conditions of weak stability are prevalent in the mid-to-high SO (with respect to our SO partitioning; 50–65°S), which might be explained by the relatively cold near-surface air overlying the relatively warm sea surface. Conditions of strong stability are prevalent elsewhere over the SO. The distribution is also less zonally symmetric than the cyclonic activity. In the high-latitude SO, the presence of sea ice might have a substantial stabilizing effect (Knight et al., 2024). The ERA5 reanalysis is also substantially more stable than ICON across the whole region.

3.2 Cloud Occurrence by Height

We used the ALCF to derive cloud occurrence by height and the total cloud fraction from observations, ICON, ERA5, and MERRA-2. The results for all campaigns individually are shown in Fig. 6. In addition, we aggregated the campaigns by calculating the averages and percentiles of all individual profiles, presented in Fig. 7. The analysis shows that the total cloud fraction (defined as the fraction of profiles with clouds at any height in the lidar cloud mask) is underestimated in ICON by about 10% and in the reanalyses by about 20%. When analyzed by height, ICON overestimates cloud occurrence below 1 km and underestimates it above; MERRA-2 underestimates cloud occurrence at all heights by up to 10%, especially near the surface; and ERA5 simulates cloud occurrence relatively well above 1 km but strongly underestimates it near the surface. We note that fog or near-surface clouds are strongly underestimated in the reanalyses (fog and clouds are both included in the cloud occurrence). As shown in Fig. 6, the biases are relatively consistent across the campaigns and longitudes. We conclude that the ICON results match the observations better than the reanalyses in this metric.

For all observations considered (Fig. 7a), the data show cloud occurrence peaking nearly at the surface, whereas the models show a higher peak (at about 500 m). The models generally underestimate the total cloud fraction by 10–20% and show a strong reduction in cloud occurrence near the surface, which is not identified in the observations. ICON and ERA5 overestimate cloud occurrence at their peak (between 0 and 1 km). Above 1 km, ICON and MERRA-2 underestimate cloud occurrence, but ERA5 is accurate to about 3% or less. The exaggerated peak in models is partly explained by the lifting condensation level (LCL) distribution, which peaks about 200 m higher in the models than in the observations (nearly at the surface), although this is not very pronounced. This is indicative of near-surface relative humidity being often close to saturation in the observations but not in the models.

When subsetted by latitude (Fig. 7b, c), we see that the low-latitude SO zone displays a stronger peak of cloud occurrence near the surface than the high-latitude SO zone, and this could be because higher latitudes have less stable atmospheric profiles. The low- and high-latitude SO zones show similar biases in models as in the general case, but ERA5 does not overestimate the peak in the low-latitude SO zone (near-surface cloud occurrence is still strongly underestimated).

When subsetted by cyclonic and non-cyclonic situations (Fig. 7d, e), we see that the cyclonic situations have a larger amount of observed cloudiness, including peak and total cloud fraction, both by about 7%. In the cyclonic situations, the model vertical profiles of cloud occurrence compare well with observations, but they peak higher by about 200 m and larger by about 8%. The reanalyses still tend to underestimate cloud occurrence above 1 km by about 5% and near the surface by about 14%. Non-cyclonic situations are similar to the general case, partially also because they form the majority of cases.

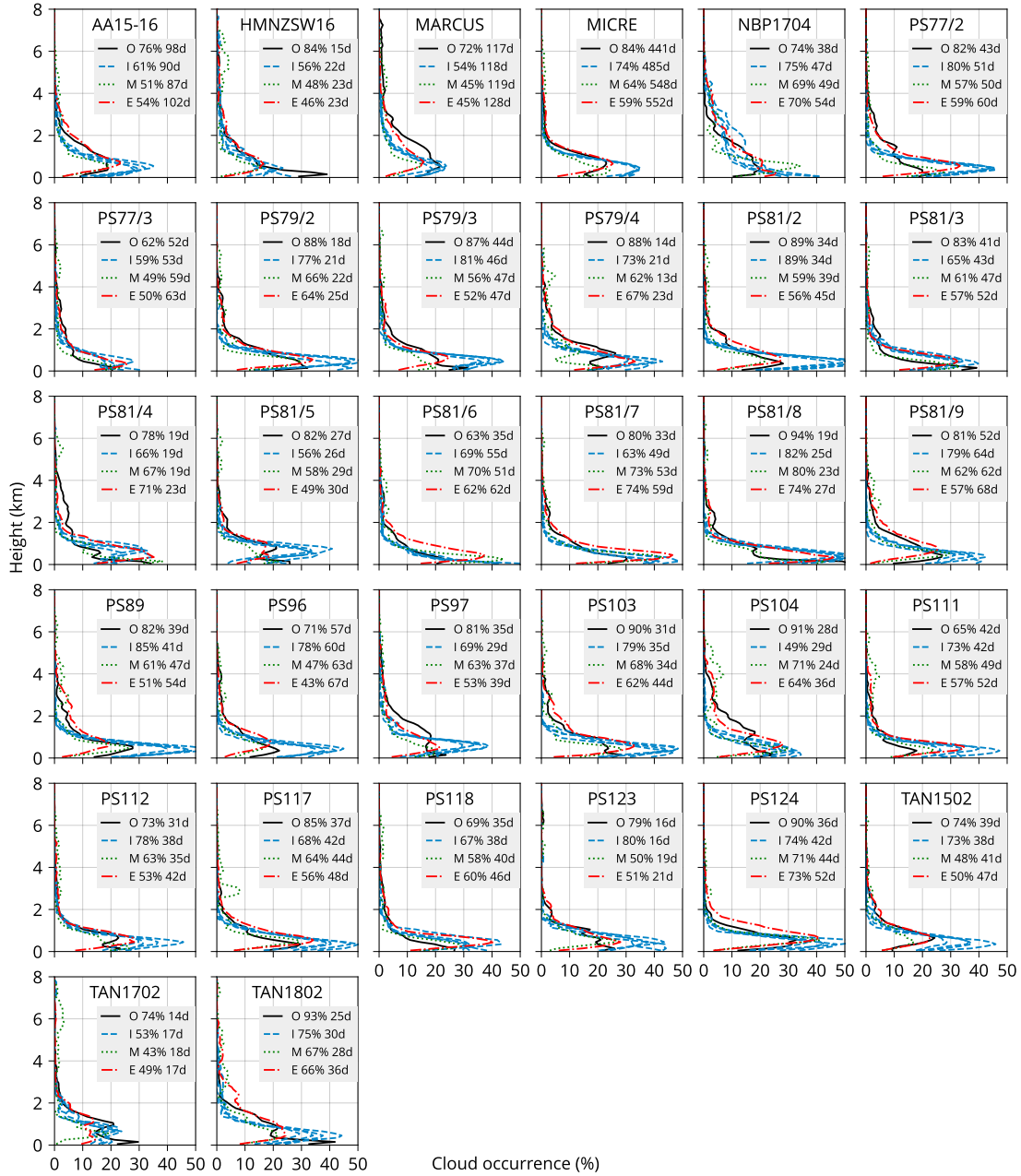


Figure 6. Cloud occurrence by height for the 31 voyages and one sub-Antarctic station (MICRE) in observations (O) and simulated by the ALCF from the ICON model (I), MERRA-2 (M), and ERA5 reanalysis data (E). The numbers in the legend indicate the total cloud fraction and the number of days of data. Multiple lines of ICON profiles are for each of the four years of model data available.

When subsetted by conditions of weak and strong stability (Fig. 7f, g), as defined in Section 2.10, we see that in situations of strong stability, cloud occurrence peaks strongly near the surface in observations, compared to situations of weak stability, where the peak is more diffuse between 0 and 1 km. It is worth mentioning that conditions of strong stability might be associated with the formation of advection fog, such as in situations of warm air advection from the north over a colder sea surface, thus inducing fog formation by cooling of the warm and humid air by the cold surface. In situations of strong stability, the models have smaller biases than in weak stability, with an overestimated peak by up to 12%, underestimated cloud occurrence above 1 km by up to 5%, and underestimated cloud occurrence near the surface by about 11%. In situations of weak stability, the bias in ICON is very pronounced, with a much larger peak in cloud occurrence at about 500 m; ERA5 underestimates cloud occurrence below 1 km (especially near the surface); and MERRA-2 underestimates cloud occurrence even more strongly.

In all situations, even when the models overestimate cloud occurrence at some altitudes, they always substantially underestimate the total cloud fraction. ICON can be generally characterized as substantially overestimating cloud occurrence below 1 km and underestimating above, underestimating the total cloud fraction, and showing the greatest biases in conditions of weak stability and non-cyclonic conditions. ICON also has a peak cloud occurrence at higher altitudes than observations (500 m vs. near the surface), and correspondingly, its LCL tends to be higher. MERRA-2 can be generally characterized as underestimating cloud occurrence at nearly all altitudes as well as the total cloud fraction, but mostly above and below 500 m (the peak at 500 m is well represented). MERRA-2 displays the largest errors relative to observations in the low-latitude SO zone and in situations of weak stability. ERA5 can be generally characterized as representing cloud occurrence correctly above about 1.5 km, overestimating between 500 m and 1 km, but underestimating near-surface cloud occurrence (0–500 m). The total cloud fraction is strongly underestimated in all situations. ERA5 has a tendency towards underestimation in the low-latitude SO zone and situations of weak stability; conversely, it overestimates in the high-latitude SO zone and conditions of strong stability.

3.3 Top of Atmosphere Radiation

In Fig. 7, we also display the mean outgoing shortwave and longwave top-of-atmosphere radiation, whose calculation is described in Section 2.8. In observations, these come from daily mean CERES measurements averaged over the voyage tracks or a station location, whereas in the models they come from daily means of TOA radiation in the model output averaged over the same location and time periods. In the free-running ICON model, the time period is mapped onto the available years, as explained in Section 2.5.

In the general case (Fig. 7a), ICON underestimates the outgoing SW radiation by 26 Wm^{-2} , and the MERRA-2 and ERA5 reanalyses overestimate it by 6 and 14 Wm^{-2} , respectively. While in ICON, this is in line with the underestimated total cloud fraction of 10%, in the reanalyses this is the opposite result to that expected from the underestimated total cloud fraction of about 20%. The likely explanation is an overestimated cloud albedo, compensating for the lack of cloud area.

We note that the radiative transfer calculations used in the lidar simulator mean that the impact of both cloud phase and cloud fraction are convolved to produce the cloud mask. Therefore, the cloud occurrence is not affected by any cloud phase biases as long as the cloud is optically thick enough to be detected, and the laser signal is not too attenuated. However, a combination of underestimated total cloud fraction and overestimated outgoing SW at TOA is indicative of an overestimated cloud albedo due to either cloud liquid and ice water content, cloud phase, droplet or ice crystal size distribution, shape or orientation of ice crystals, or cloud overlap.

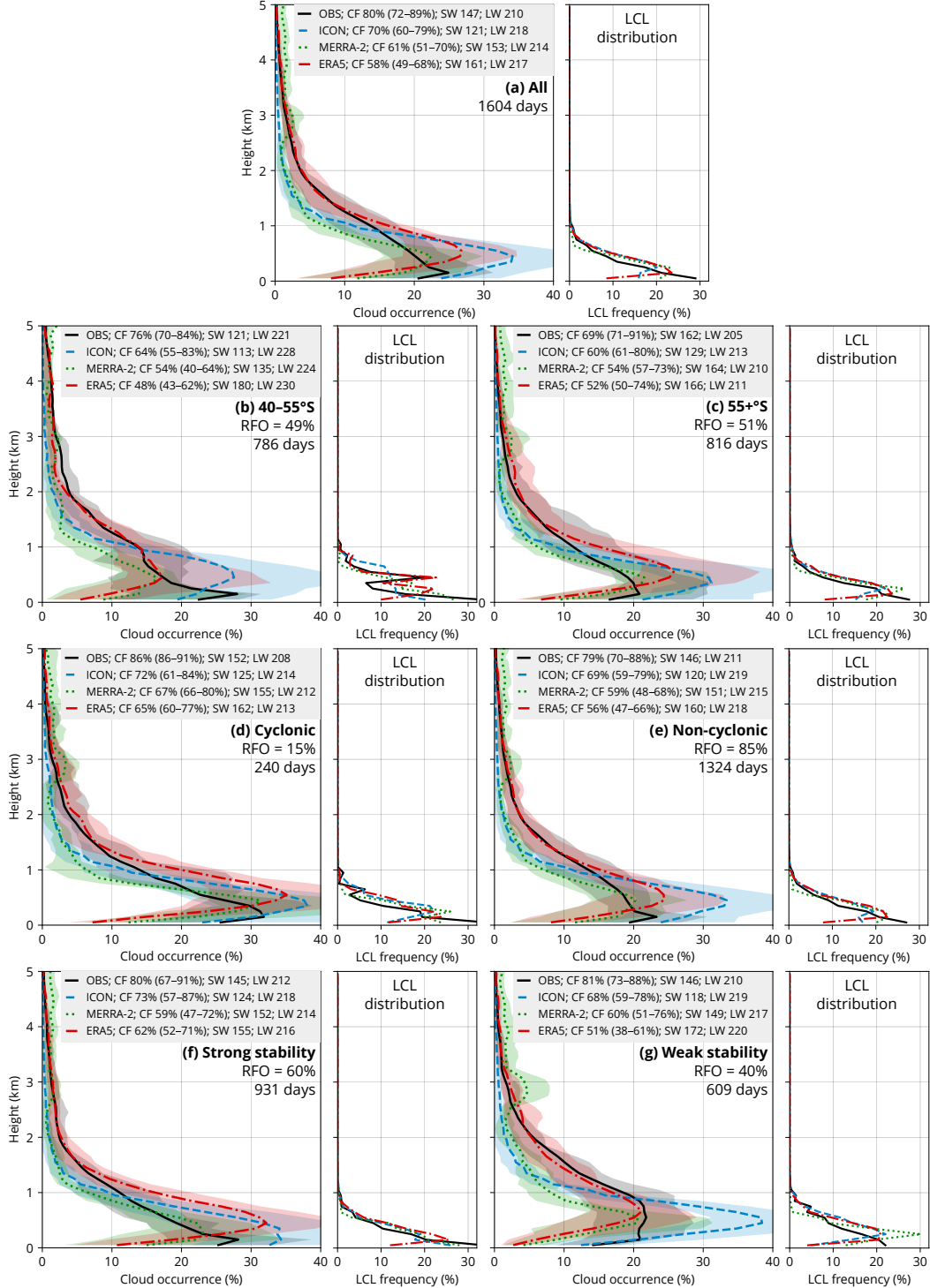


Figure 7. Cloud occurrence by height calculated as the average of all voyages and stations and lifting condensation level (LCL) distribution. The LCL is derived from radiosonde profiles and equivalent model profiles, which were not available for all voyages and times. The total cloud fraction (CF), average shortwave (SW), and longwave (LW) and the relative frequency of occurrence (RFO) are shown. The bands are the 16th–84th percentile, calculated from the set of all voyages and stations.

In contrast, LW radiation has much smaller biases than SW radiation, which is expected due to the prevailing low-level clouds having similar temperature as the surface. In ICON, the outgoing LW radiation is overestimated by 8%, which could be caused by an underestimated total cloud fraction exposing a larger sea surface area to cooling to space, which is typically warmer than the atmospheric temperature at 0–2 km, where most of the clouds are located. In the MERRA-2 and ERA5 reanalyses, the LW biases are also slightly positive, 4 and 7 Wm^{-2} , respectively. This is again in line with the underestimated total cloud fraction by about 20%. However, if the clouds are too thick, as expected from the SW results, this might also provide a compensating effect, in which too small a cloud area is counteracted by greater thermal emissivity, thus reducing the outgoing LW radiation more relative to thinner clouds. For thin clouds, the outgoing TOA LW radiation originates both from the warmer surface (partly blocked by the clouds) and the clouds, whereas for thick clouds, the outgoing TOA LW radiation originates mostly from the colder-than-surface clouds.

In all the subsets (Fig. 7b–g), the same type of biases are observed, namely the outgoing SW radiation is underestimated in ICON and overestimated in MERRA-2 and ERA5, and the outgoing LW radiation is overestimated in all the models. Even though the total cloud fraction is lower by 7% over the high-latitude SO than the low-latitude SO, the outgoing SW radiation is much greater by 41 Wm^{-2} , implying a much greater cloud albedo over the high-latitude SO. The ICON model output displays the same contrast between these two regions in the total cloud fraction and SW radiation, but the outgoing SW radiation difference between the regions is much smaller (16 Wm^{-2}). The reanalyses do not show this type of contrast between the regions. The physical reason for this might be that the prevalence of fog or low-level clouds over the low-latitude SO and their relative lack over the high-latitude SO in observations is not reproduced in the models (Fig. 7b–c).

3.4 Cloud Cover

We also analyzed the daily cloud cover (total cloud fraction) distribution. This is a measure of cloudiness, irrespective of height, calculated over the course of a day (UTC). A cloud detected at any height means that the lidar profile was classified as cloudy; otherwise, it was classified as a clear sky. When all profiles in a day are taken together, the cloud cover for the day is defined as the fraction of cloudy profiles in the total number of profiles, expressed in oktas (multiples of 1/8). The same calculation is done for the lidar observations as for the simulated lidar profiles. We use the term “okta” independently of its use in instantaneous synoptic observations, and here it simply means 1/8 (0.125%) of the daily cloud cover.

In Fig. 8 we show the results for the same subsets of data as in Section 3.2. Observations display the highest proportion of high cloud cover values (5–8 oktas), peaking at 7 oktas. This pattern is not represented by ICON or either reanalysis. While ICON is closest to matching the observed distribution, it tends to be 1 okta clearer than the observations, peaking at 6 oktas, and substantially underestimating days with 8 oktas. Overall, the reanalyses show results similar to each other, underestimating cloud cover by about 2 oktas and strongly underestimating days with 7 and 8 oktas. Of the two reanalyses, MERRA-2 has slightly higher cloud cover than ERA5, by about 6% at 6 oktas, which makes it more consistent with observations.

When analyzed by subsets, observations in the cyclonic subset show the highest cloud cover, with 8 oktas occurring on one half of such days (Fig. 8d). This sensitivity to cyclonic conditions is not observed in ICON or the reanalyses. Interestingly, clear sky days (0 oktas) also have a local maximum peaking at about 15% in this subset. When we contrast the low- and high-latitude zones, we see that the high-latitude zone tends to have greater cloud cover, peaking at 8 oktas (Fig. 8c). The high-latitude zone also has

almost no clear sky or small cloud cover cases (0–4 oktas). ICON and the reanalyses represent this characteristic of the distribution well for 0–3 oktas, but otherwise show biases similar to the general case. One of the greatest biases is present in ERA5 in the subset of weak stability, in which ERA5 peaks at 3 oktas, while the observations peak at 7 oktas and show negligible cloud cover below 5 oktas.

3.5 Thermodynamic Profiles

In order to examine the potential link in the cloud biases to the local physical conditions, we analyzed about 2300 radiosonde profiles south of 40°S from the 24 RV *Polarstern* voyages, MARCUS, NBP1704, TAN1702, and TAN1802. Spatially and temporally colocated profiles were taken from ICON and the reanalyses. Because the time period covered by the ICON model output (2021–2024) was different from the time period covered by the observations (2010–2021), when comparing with the model, we first had to remap the observation time to model time by taking the same time relative to the start of the year. Consequently, we also had four virtual/model profiles (one for each year of 2021–2024) for each observed profile. The profiles were partitioned into the same subsets as above (Sections 3.2 and 3.4). We focus on comparing virtual potential temperature (θ_v) due to its role in low-level tropospheric stability, being one of the primary factors affecting shallow convection and the associated low-level cloud formation and dissipation. The observed and model profiles of virtual potential temperature are shown in Fig. 9.

Overall, the mean θ_v is accurate to within 0.5 K in ICON and MERRA-2, except for ICON being colder by up to 2.5 K in the mid-to-high troposphere (less stable) (Fig. 9a). Larger differences exist, however, in the 40–55°S zone, where ICON is colder by about 5 K at higher altitudes (Fig. 9b). In other subsets, the bias is relatively small. MERRA-2 and ERA5 are very close to the observations, possibly due to a high accuracy of assimilation of this quantity. Notably, the variability of virtual potential temperature (as represented by the percentiles) is much smaller in ICON than in the observations. This indicates that the model's internal variability in the lower-tropospheric thermodynamic conditions in the SO is smaller than in reality.

Relative humidity displays much larger biases. In all subsets, ICON is too humid in the first 1 km by about 5% but very accurate above, except for the 40–55°S zone and conditions of weak stability (Fig. 9b, g), where it is too dry between about 1 and 3 km. MERRA-2, on the other hand, is more humid than observations at all altitudes and in all subsets, by up to about 20% at 5 km. Even though the mean near-surface relative humidity is similar to the observations (Fig. 9), the distribution in observation is more spread out across both high and low values, and thus observations have a greater prevalence of relative humidity close to 100% and thus LCL located at the surface (Fig. 7a). In our calculations, LCL is an exclusive function of near-surface temperature, near-surface relative humidity, and surface pressure.

4 Limitations of this Study

Let us consider the main limitations of the presented results. The spatial coverage of our dataset does not include most parts of the Indian Ocean and Pacific Ocean sectors of the SO. Even though climatological features of the SO are typically relatively uniform zonally, variations exist, such as those related to the Antarctic Peninsula and the southern tip of South America. The voyages were mostly undertaken in the Austral summer months and only rarely in the winter months, due to the poor accessibility of this region during winter. Therefore, our results are likely representative of summer and, to a lesser extent, spring and autumn conditions.

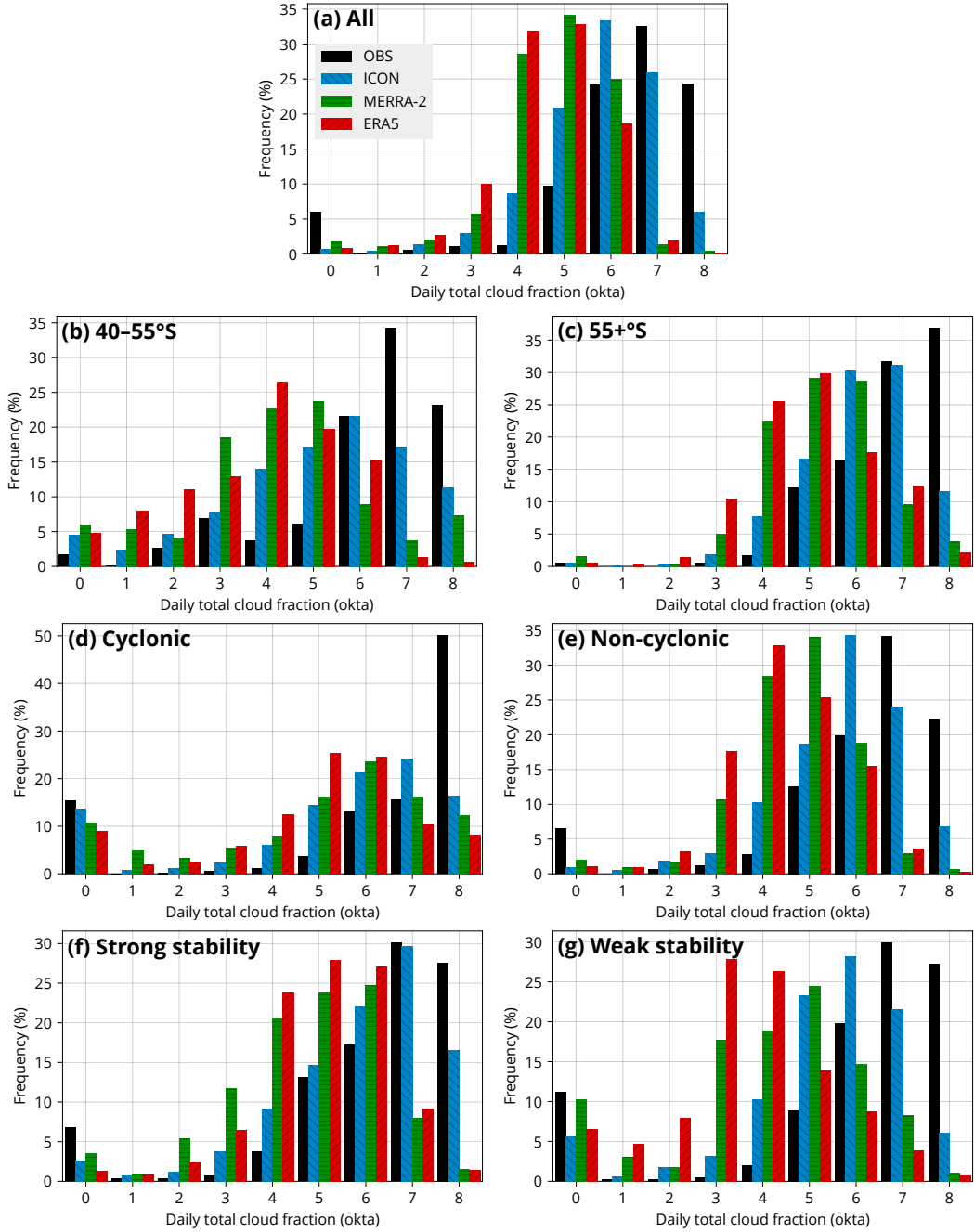


Figure 8. Daily total cloud fraction histograms calculated as the average of all voyage and station histograms. The total cloud fraction of a day (UTC) is calculated as a fraction of cloudy (based on the cloud mask) observed (OBS) or simulated lidar profiles. The models and subsets are as in Fig. 7.

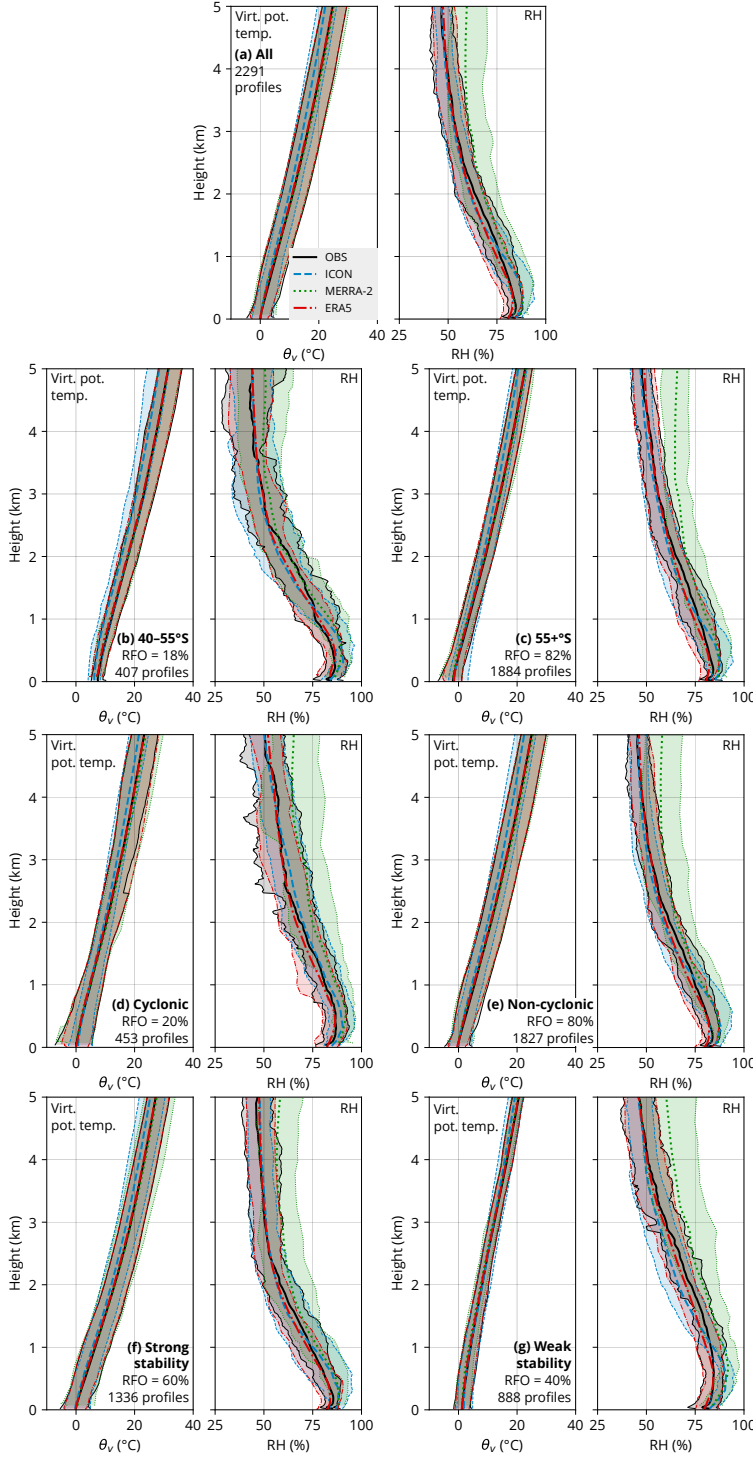


Figure 9. Virtual potential temperature (virt. pot. temp.; θ_v) and relative humidity (RH) determined from radiosonde launches and co-located profiles in ICON, ERA5, and MERRA-2 in subsets as in Fig. 7. The solid lines are the average calculated from the averages of every individual voyage and station. The bands span the 16th–84th percentiles, calculated from the distribution of the voyage and station averages. Shown is also the relative frequency of occurrence and the number of profiles in each subset.

The time period of ICON is relatively short, with only four full years of simulation available. Moreover, the simulation is free-running and ocean-coupled, which means that observations had to be temporally mapped to this time period (at the same time relative to the start of the year) for the comparison. For these reasons, one can expect the results to be slightly different due to reasons unrelated to model biases, such as different weather conditions, partially accounted for by the cyclone and stability subsetting, and the phase of climate oscillations such as the ENSO in the observations and the model. The interannual variability in cloud occurrence in ICON can be seen in Fig. 6, where each year in ICON is represented by a separate line. The interannual variability tends to be substantially smaller than the biases and thus is unlikely to have a strong impact on the main findings.

Ground-based lidar observations are affected by attenuation by thick cloud layers, and for this reason the results are most representative of boundary layer clouds, while higher-level clouds are only occasionally visible to the lidar when boundary layer clouds are not present. Ground-based lidar observations can be regarded as superior to satellite lidar observations for low-level clouds, which are predominant in this region, while mid- and high-level clouds are likely better sampled by satellite observations (McErlich et al., 2021). Near-surface lidar retrievals (~ 100 m) are affected by uncertainties related to incomplete overlap, signal saturation (dead time), and after-pulse effect corrections (Kuma et al., 2021).

We have attempted to remove lidar profiles with precipitation, which could not be properly simulated with the lidar simulator (Section 2.9). However, the approach was limited by the relatively low sensitivity of the ANN (65%) and the fact that we had to choose a fixed threshold for surface precipitation flux in the model and reanalyses, which might not correspond to detection by the ANN applied to observations. We also made no attempt to remove profiles with precipitation that did not reach the surface. The above reasons may result in an artificial bias in the comparison, though we expect this to be much smaller than the identified model biases.

5 Discussion and Conclusions

We analyzed a total of about 2400 days of lidar and 2300 radiosonde observations from 31 voyages/campaigns and the Macquarie Island subantarctic station, covering the Atlantic, Australian, and New Zealand sectors of the SO over the span of 10 years. This dataset, together with the use of a ground-based lidar simulator, provided a comprehensive basis for evaluating SO cloud and thermodynamic profile biases in the GSRM ICON and the ERA5 and MERRA-2 reanalyses. Our analysis provides a unique evaluation perspective different from satellite observations – one that we argue is more suitable for evaluating boundary layer clouds, which are predominant in this region. Furthermore, we subsetted our dataset by low and high latitude bands, cyclonic activity, and stability in order to identify how these conditions influence the biases.

Our main finding corroborates previous findings of large boundary layer cloud biases in models and their subsequent effect on the radiative transfer. For example, low- and mid-level clouds in the cold-air sector of cyclones were identified as being responsible for most of the SW bias in Bodas-Salcedo et al. (2012). This understanding was refined in Bodas-Salcedo et al. (2014), which highlighted that the SW bias was associated with an incorrectly simulated mid-level cloud regime, which occurred in regions where clouds with tops at mid-level and low-levels occurred. Our results align less well with more recent work by Ramadoss et al. (2024), which shows persistent shortwave radiative biases over the Southern Ocean are associated with incorrect cloud phase representation. While Fiddes et al. (2024) suggest biases in the liquid water path are the largest contributor to the cloud radiative bias over the Southern Ocean. Our general finding applies to the new GSRM ICON, but the biases are generally lower than in the reanaly-

720 ses, despite the reanalyses having the advantage of assimilation of the observed mete-
 721 orological conditions. The GSRM has, on the other hand, the advantage of a much higher
 722 spatial resolution and, to a limited extent, explicit calculation of traditionally subgrid-
 723 scale processes such as convection.

724 We show that relative to ERA5, the distribution and strength of cyclonic activity
 725 over the SO is well represented in ICON, but it displays lower values of LTS. The lat-
 726 ter is also manifested in the radiosonde profile comparison, showing that the virtual po-
 727 tential temperature profiles in ICON are less stable than in the observations over low-
 728 latitude SO.

729 The 31 voyages and a station show remarkably similar biases in cloud occurrence
 730 by height in the lidar comparison, which indicates that common underlying causes for
 731 the biases exist regardless of longitude and season. ICON underestimates the total cloud
 732 fraction by about 10%, with an overestimation of clouds below 2 km and an underesti-
 733 mation of clouds above 2 km. The reanalyses also underestimate the total cloud frac-
 734 tion by about 20%. ERA5 overestimates cloud below 1 km but underestimates near-surface
 735 cloud or fog. ICON strongly overestimates the peak of cloud occurrence at about 500
 736 m, which might be explained by the radiosonde comparison, showing that it is too moist
 737 at around this height. Similar to our results, Cesana et al. (2022) showed that CMIP6
 738 models also tend to underestimate cloud occurrence above 2 km over the SO, although
 739 their analysis in this case was limited to liquid clouds.

740 Compared to lidar observations, the daily cloud cover tends to be about 1 okta lower
 741 in ICON and 2 oktas lower in the reanalyses. Conditions of weak stability are associated
 742 with some of the greatest biases, especially in ERA5. The models also underestimate the
 743 cloud cover very strongly in cyclonic conditions, which are very cloudy in the observa-
 744 tions (8 oktas), but much less so in the models. Similarly, McErlich et al. (2023) found
 745 a 40% underestimation of cloud liquid water in cyclones over the SO in ERA5, despite
 746 total column water vapor simulated much more accurately (5% underestimation).

747 The radiosonde observations indicate that the LCL is too high in ICON and reanal-
 748 yses, which is probably responsible for the higher peak of clouds in the models and the
 749 lack of near-surface clouds or fog. The radiosonde comparison, however, does not seem
 750 to explain cloud biases at higher altitudes, which is perhaps suggestive of biases in the
 751 influence of the liquid water path in the models relative to reality. MERRA-2 is too moist
 752 at all heights. ICON also exhibits smaller internal variability than the radiosonde ob-
 753 servations. Overall, the radiosonde comparison only partially explains the identified cloud
 754 biases, and other physical causes are likely contributing. This warrants further investi-
 755 gation, especially of ocean–atmosphere fluxes, shallow convection, and boundary layer
 756 turbulence. The lack of parameterized subgrid-scale convection in ICON could be a sub-
 757 stantial issue even at the 5-km resolution.

758 The relationship between cloud biases and radiation has a number of notable fea-
 759 tures. Perhaps unsurprisingly, the reanalyses exhibit the too few, too bright bias pre-
 760 viously identified in models. In our results, this is characterized by outgoing TOA SW
 761 radiation similar to or higher than in the satellite observations, while at the same time
 762 total cloud fraction is substantially underestimated relative to the ground-based lidar
 763 observations. This feature seems to be much more pronounced in ERA5 than in MERRA-
 764 2. On the other hand, this relationship is not present in ICON. This model generally pre-
 765 dicts smaller outgoing TOA SW radiation and smaller total cloud fraction than obser-
 766 vations, and the deficit of outgoing TOA SW radiation is approximately proportional
 767 to the deficit of the total cloud fraction. While this might be a welcome feature and an
 768 improvement over previous models, it does mean that the outgoing TOA SW radiation
 769 is overall underestimated instead of being compensated by a higher cloud albedo. This
 770 can, of course, lead to undesirable secondary effects such as overestimated solar heat-
 771 ing of the sea surface, among other factors responsible for SO SST biases in climate mod-

772 els (Q. Zhang et al., 2023; Luo et al., 2023; Hyder et al., 2018). To some extent, the cloud
 773 albedo might be reduced in the model artificially by the application of an inhomogeneity
 774 factor to lower cloud liquid water in the radiative transfer calculations (Sec. 2.5).

775 The results imply that SO cloud biases are still a substantial issue even in the km-
 776 scale resolution ICON model, even though an improvement over the lower-resolution re-
 777 analyses is notable. More effort is therefore needed to improve the model cloud simu-
 778 lations in this understudied region. However, this analysis suggests that the transition
 779 from models with parameterized convection and clouds to storm-resolving models might
 780 not solve these biases without additional effort. Evaluation of ocean–atmosphere heat,
 781 moisture, and momentum fluxes against in-situ observations over the SO and compar-
 782 ison of GSRM simulations against large-eddy simulations are two potential avenues for
 783 future research that could elucidate the physical mechanisms behind the biases, in ad-
 784 dition to the more common efforts in SO cloud microphysics and precipitation evalua-
 785 tion.

786 Open Research Section

787 The RV *Polarstern* datasets are openly available on Pangaea (<https://pangaea.de>), as listed in Table 2. The MARCUS and MICRE datasets are openly available from
 788 ARM (<https://www.arm.gov>). The MERRA-2 data are openly available from the NASA
 789 Goddard Earth Sciences (GES) Data and Information Services Center (DISC) (<https://disc.gsfc.nasa.gov/datasets?project=MERRA-2>). The ERA5 data are openly avail-
 790 able from the Copernicus Climate Data Store (CDS) (<https://cds.climate.copernicus.eu>). The ICON data are available on the Levante cluster of the DKRZ (<https://www.dkrz.de/en/systems/hpc/hlre-4-levante>) after registration at <https://luv.dkrz.de/register/>. The CERES products are openly available from the project website (<https://ceres.larc.nasa.gov>) and the NASA Atmospheric Science Data Centre (<https://asdc.larc.nasa.gov/project/CERES>). The TAN1802 data are openly available on Zenodo
 791 (Kremser et al., 2020). The code for performing the presented analysis, precipitation de-
 792 tection, and a custom version of the ALCF using for our analysis are open-source and
 793 available at <https://github.com/peterkuma/icon-so-2024>, <https://github.com/peterkuma/alcf-precip>, and <https://github.com/peterkuma/icon-so-2024-alcf>,
 794 respectively. The remaining voyage data (AA15-16, HMNZSW16, NBP1704, TAN1502,
 795 and TAN1702) are openly available on Zenodo (McDonald, Alexander, et al., 2024). The
 796 Natural Earth dataset is openly available from <https://www.natural-earth-data.com>.

805 Acknowledgments

806 PK, FB, and the nextGEMS project received funding from the European Union’s
 807 Horizon 2020 research and innovation program under a grant agreement no. 101003470.
 808 FB received funding from the Wenner-Gren Foundation and the Swedish e-Science Re-
 809 search Centre. The work of GM was supported by the United States (U.S.) Department
 810 of Energy Award DE-SC0021159. Supercomputing resources were provided by the DKRZ
 811 (project 1125 ICON-development) and the National Academic Infrastructure for Super-
 812 computing in Sweden (allocation 2023/22-202). The data collection by the University
 813 of Canterbury was funded by the Deep South National Science Challenge Clouds and
 814 Aerosols project. Data collection on the AA15-16 voyages was funded by the Australian
 815 Antarctic Science project (grant no. 4292). We acknowledge the contribution of Thorsten
 816 Mauritsen to funding acquisition and project management. We acknowledge the RV *Po-*
 817 *larstern* datasets provided by the Alfred Wegener Institute and Pangaea, the AA15-16
 818 dataset provided by the Australian Antarctic Division (AAD) and University of Can-
 819 terbury (UC), the RV *Tangaroa* datasets provided by the National Institute of Water
 820 and Atmospheric Research and UC, the NBP1704 dataset provided by the National Sci-
 821 ence Foundation, Cooperative Institute for Research in Environmental Sciences, Univer-

sity of Colorado and UC, the HMNZSW16 dataset provided by the Royal New Zealand Navy and UC, the MARCUS dataset provided by ARM and AAD, and the MICRE dataset provided by ARM, the Australian Bureau of Meteorology, and AAD. Technical, logistical, and ship support for MARCUS and MICRE were provided by the AAD through Australian Antarctic Science projects 4292 and 4387, and we thank Steven Whiteside, Lloyd Symonds, Rick van den Enden, Peter de Vries, Chris Young, Chris Richards, Andrew Klekociuk, John French, Terry Egan, Nick Cartwright, and Ken Barrett for all of their assistance. We thank the scientific staff, the crew, and everyone involved in collecting data on the voyages and stations, especially Gert König-Langlo, Holger Schmithüsen, Roger Marchand, Peter Guest, Kelly Schick, Jamie Halla, and Mike J. Harvey (†). We thank Loretta Preis for providing additional RV *Polarstern* data. We acknowledge the ICON model output provided by the nextGEMS project, Deutscher Wetterdienst, Max-Planck-Institute for Meteorology, DKRZ, Karlsruhe Institute of Technology, and Center for Climate Systems Modeling; the reanalysis dataset ERA5 provided by the Copernicus Climate Change Service; MERRA-2 provided by the Global Modeling and Assimilation Office; CERES datasets provided by the NASA Langley Atmospheric Science Data Center Distributed Active Archive Center; and the Natural Earth dataset provided by naturalearthdata.com. Last but not least, we acknowledge the use of open-source software: Python, Cython (Behnel et al., 2011), TensorFlow (Abadi et al., 2016), Devuan GNU+Linux, parallel (Tange, 2011), NumPy (Harris et al., 2020), SciPy (Virtanen et al., 2020), Matplotlib (Hunter, 2007), cartopy (Met Office, 2010), pyproj, Inkscape, Bash, GNU Fortran, HDF (Folk et al., 1999), and NetCDF (Rew & Davis, 1990). We dedicate this study to the memory of Mike J. Harvey, who very substantially contributed to obtaining the atmospheric observations on the RV *Tangaroa* voyages used in this study.

846 References

- 847 Abadi, M., Agarwal, A., Barham, P., Brevdo, E., Chen, Z., Citro, C., ... Zheng, X.
 848 (2015). *TensorFlow: Large-scale machine learning on heterogeneous systems*
 849 [*Software*]. Retrieved from <https://www.tensorflow.org>
 850 Abadi, M., Barham, P., Chen, J., Chen, Z., Davis, A., Dean, J., ... Zheng, X.
 851 (2016). TensorFlow: A system for large-scale machine learning. In *Proceedings*
 852 *of the 12th usenix conference on operating systems design and implementation*
 853 (pp. 265–283). USA: USENIX Association.
 854 Ackley, S. F., Stammerjohn, S., Maksym, T., Smith, M., Cassano, J., Guest, P., ...
 855 Parno, J. (2020). Sea-ice production and air/ice/ocean/biogeochemistry interactions
 856 in the Ross Sea during the PIPERS 2017 autumn field campaign.
Annals of Glaciology, 61(82), 181–195. doi: 10.1017/aog.2020.31
 857 Bacmeister, J. T., Suarez, M. J., & Robertson, F. R. (2006). Rain reevaporation,
 858 boundary layer–convection interactions, and pacific rainfall patterns in
 859 an AGCM. *Journal of the Atmospheric Sciences*, 63(12), 3383–3403. doi:
 860 10.1175/JAS3791.1
 861 Behnel, S., Bradshaw, R., Citro, C., Dalcin, L., Seljebotn, D. S., & Smith, K. (2011).
 862 Cython: The best of both worlds. *Computing in Science Engineering*, 13(2),
 863 31–39. doi: 10.1109/MCSE.2010.118
 864 Bender, F. A.-M., Engström, A., Wood, R., & Charlson, R. J. (2017). Evaluation of
 865 hemispheric asymmetries in marine cloud radiative properties. *Journal of Climate*,
 866 30(11), 4131–4147. doi: 10.1175/JCLI-D-16-0263.1
 867 Bodas-Salcedo, A., Webb, M., Bony, S., Chepfer, H., Dufresne, J.-L., Klein, S.,
 868 ... others (2011). COSP: Satellite simulation software for model assessment.
Bulletin of the American Meteorological Society, 92(8), 1023–1043. doi:
 869 10.1175/2011BAMS2856.1
 870 Bodas-Salcedo, A., Williams, K. D., Field, P. R., & Lock, A. P. (2012). The surface
 871 downwelling solar radiation surplus over the Southern Ocean in the Met Office
 872 model: The role of midlatitude cyclone clouds. *Journal of Climate*, 25(21),
 873

- 875 7467–7486. doi: 10.1175/jcli-d-11-00702.1
- 876 Bodas-Salcedo, A., Williams, K. D., Ringer, M. A., Beau, I., Cole, J. N. S.,
 877 Dufresne, J. L., ... Yokohata, T. (2014). Origins of the solar radiation bi-
 878 ases over the Southern Ocean in CMIP2 models. *Journal of Climate*, 27(1),
 879 41–56. doi: 10.1175/jcli-d-13-00169.1
- 880 Boebel, O., & Rohardt, G. (2013). *Continuous thermosalinograph oceanogra-
 881 phy along POLARSTERN cruise track ANT-XXIX/2 [Dataset]*. PANGA-
 882 GAEA. Retrieved from <https://doi.org/10.1594/PANGAEA.808838> doi:
 883 10.1594/PANGAEA.808838
- 884 Boebel, O., & Rohardt, G. (2016). *Continuous thermosalinograph oceanography
 885 along POLARSTERN cruise track PS89 (ANT-XXX/2) [Dataset]*. PANGA-
 886 GAEA. Retrieved from <https://doi.org/10.1594/PANGAEA.858884> doi:
 887 10.1594/PANGAEA.858884
- 888 Boebel, O., & Rohardt, G. (2018). *Continuous thermosalinograph oceanography
 889 along POLARSTERN cruise track PS103 (ANT-XXXII/2) [Dataset]*. PANGA-
 890 GAEA. Retrieved from <https://doi.org/10.1594/PANGAEA.889513> doi: 10
 891 .1594/PANGAEA.889513
- 892 Boebel, O., & Rohardt, G. (2019). *Continuous thermosalinograph oceanography
 893 along POLARSTERN cruise track PS117 [Dataset]*. PANGAEA. Retrieved
 894 from <https://doi.org/10.1594/PANGAEA.905562> doi: 10.1594/PANGAEA
 895 .905562
- 896 Bohrmann, G., & Rohardt, G. (2013). *Continuous thermosalinograph oceanogra-
 897 phy along POLARSTERN cruise track ANT-XXIX/4 [Dataset]*. PANGAEA.
 898 Retrieved from <https://doi.org/10.1594/PANGAEA.810678> doi: 10.1594/
 899 PANGAEA.810678
- 900 Bosilovich, M. G., Lucchesi, R., & Suarez, M. (2016). MERRA-2: File specifica-
 901 tion [Computer software manual]. Greenbelt, Maryland 20771, USA. Retrieved
 902 from http://gmao.gsfc.nasa.gov/pubs/office_notes (GMAO Office Note
 903 No. 9 (Version 1.1))
- 904 Bubnová, R., Hello, G., Bénard, P., & Geleyn, J.-F. (1995). Integration of the
 905 fully elastic equations cast in the hydrostatic pressure terrain-following co-
 906 ordinate in the framework of the ARPEGE/Aladin NWP system. *Monthly
 907 Weather Review*, 123(2), 515–535. doi: 10.1175/1520-0493(1995)123<0515:
 908 IOTFEE>2.0.CO;2
- 909 Caldwell, P. M., Terai, C. R., Hillman, B., Keen, N. D., Bogenschutz, P., Lin, W.,
 910 ... Zender, C. S. (2021). Convection-permitting simulations with the E3SM
 911 global atmosphere model. *Journal of Advances in Modeling Earth Systems*,
 912 13(11), e2021MS002544. doi: 10.1029/2021MS002544
- 913 Cesana, G. V., Khadir, T., Chepfer, H., & Chiriaco, M. (2022). Southern Ocean so-
 914 lar reflection biases in CMIP6 models linked to cloud phase and vertical struc-
 915 ture representations. *Geophysical Research Letters*, 49(22), e2022GL099777.
 916 doi: 10.1029/2022GL099777
- 917 Chepfer, H., Bony, S., Winker, D., Cesana, G., Dufresne, J. L., Minnis, P., ... Zeng,
 918 S. (2010). The GCM-Oriented CALIPSO Cloud Product (CALIPSO-GOCCP).
 919 *Journal of Geophysical Research: Atmospheres*, 115(D4), D00H16. doi:
 920 10.1029/2009JD012251
- 921 Doelling, D. R., Loeb, N. G., Keyes, D. F., Nordeen, M. L., Morstad, D., Nguyen,
 922 C., ... Sun, M. (2013). Geostationary enhanced temporal interpolation for
 923 CERES flux products. *Journal of Atmospheric and Oceanic Technology*, 30(6),
 924 1072–1090. doi: 10.1175/JTECH-D-12-00136.1
- 925 Doelling, D. R., Sun, M., Nguyen, L. T., Nordeen, M. L., Haney, C. O., Keyes,
 926 D. F., & Mlynczak, P. E. (2016). Advances in geostationary-derived longwave
 927 fluxes for the CERES synoptic (SYN1deg) product. *Journal of Atmospheric
 928 and Oceanic Technology*, 33(3), 503–521. doi: 10.1175/JTECH-D-15-0147.1
- 929 Dorschel, B., & Rohardt, G. (2019). *Continuous thermosalinograph oceanography*

- 930 *along POLARSTERN cruise track PS118 [Dataset]*. PANGAEA. Retrieved
 931 from <https://doi.org/10.1594/PANGAEA.905608> doi: 10.1594/PANGAEA
 932 .905608
- 933 DYAMOND author team. (2024). *DYAMOND Initiative*. Retrieved from
 934 <https://www.esiwace.eu/the-project/past-phases/dyamond-initiative>
 935 (Accessed on 19 June 2024)
- 936 ECMWF. (2019, 11). *Copernicus Climate Change Service (C3S) (2017): ERA5:*
 937 *Fifth generation of ECMWF atmospheric reanalyses of the global climate*.
 938 Copernicus Climate Change Service Climate Data Store (CDS). Retrieved
 939 from <https://cds.climate.copernicus.eu/cdsapp#!/home> doi:
 940 10.24381/cds.bd0915c6
- 941 ECMWF. (2023). *IFS documentation CY48R1*. Shinfield Park, Reading, RG2
 942 9AX, United Kingdom: Author. Retrieved from <https://www.ecmwf.int/en/publications/ifs-documentation> (Accessed on 4 December 2024)
- 943 Eyring, V., Bony, S., Meehl, G. A., Senior, C. A., Stevens, B., Stouffer, R. J., &
 944 Taylor, K. E. (2016). Overview of the Coupled Model Intercomparison Project
 945 Phase 6 (CMIP6) experimental design and organization. *Geoscientific Model
 946 Development*, 9(5), 1937–1958. doi: 10.5194/gmd-9-1937-2016
- 947 Fahrbach, E., & Rohardt, G. (2011). *Continuous thermosalinograph oceanogra-*
 948 *phy along POLARSTERN cruise track ANT-XXVII/2 [Dataset]*. PANGAEA.
 949 Retrieved from <https://doi.org/10.1594/PANGAEA.760120> doi: 10.1594/
 950 PANGAEA.760120
- 951 Fiddes, S. L., Mallet, M. D., Protat, A., Woodhouse, M. T., Alexander, S. P., &
 952 Furtado, K. (2024). A machine learning approach for evaluating Southern
 953 Ocean cloud radiative biases in a global atmosphere model. *Geoscientific
 954 Model Development*, 17(7), 2641–2662. doi: 10.5194/gmd-17-2641-2024
- 955 Fiddes, S. L., Protat, A., Mallet, M. D., Alexander, S. P., & Woodhouse, M. T.
 956 (2022). Southern Ocean cloud and shortwave radiation biases in a nudged cli-
 957 mate model simulation: does the model ever get it right? *Atmospheric Chem-
 958 istry and Physics*, 22(22), 14603–14630. doi: 10.5194/acp-22-14603-2022
- 959 Folk, M., McGrath, R., & Yeager, N. (1999). HDF: an update and future directions.
 960 In *Ieee 1999 international geoscience and remote sensing symposium. igarss'99*
 961 (*cat. no.99ch36293*) (Vol. 1, pp. 273–275). doi: 10.1109/IGARSS.1999.773469
- 962 Forbes, R. M., & Ahlgrimm, M. (2014). On the representation of high-latitude
 963 boundary layer mixed-phase cloud in the ECMWF global model. *Monthly
 964 Weather Review*, 142(9), 3425–3445. doi: 10.1175/MWR-D-13-00325.1
- 965 Gelaro, R., McCarty, W., Suárez, M. J., Todling, R., Molod, A., Takacs, L., ...
 966 others (2017). The modern-era retrospective analysis for research and appli-
 967 cations, version 2 (MERRA-2). *Journal of Climate*, 30(14), 5419–5454. doi:
 968 10.1175/JCLI-D-16-0758.1
- 969 Giorgetta, M. A., Brokopf, R., Crueger, T., Esch, M., Fiedler, S., Helmert, J., ...
 970 Stevens, B. (2018). ICON-A, the atmosphere component of the ICON Earth
 971 system model: I. model description. *Journal of Advances in Modeling Earth
 972 Systems*, 10(7), 1613–1637. doi: 10.1029/2017MS001242
- 973 Gohl, K., & Rohardt, G. (2018). *Continuous thermosalinograph oceanography along*
 974 *POLARSTERN cruise track PS104 (ANT-XXXII/3) [Dataset]*. PANGAEA.
 975 Retrieved from <https://doi.org/10.1594/PANGAEA.889515> doi: 10.1594/
 976 PANGAEA.889515
- 977 Grundner, A. (2023). *Data-driven cloud cover parameterizations for the ICON Earth*
 978 *system model using deep learning and symbolic regression* (Doctoral disserta-
 979 tion, University of Bremen, Bremen, Germany). doi: 10.26092/elib/2821
- 980 Grundner, A., Beucler, T., Gentine, P., Iglesias-Suarez, F., Giorgetta, M. A.,
 981 & Eyring, V. (2022). Deep learning based cloud cover parameteriza-
 982 tion for ICON. *Journal of Advances in Modeling Earth Systems*, 14(12),
 983 e2021MS002959. doi: 10.1029/2021MS002959

- 985 Gutt, J., & Rohardt, G. (2013). *Continuous thermosalinograph oceanography along*
 986 *POLARSTERN cruise track ANT-XXIX/3 [Dataset]*. PANGAEA. Retrieved
 987 from <https://doi.org/10.1594/PANGAEA.809727> doi: 10.1594/PANGAEA
 988 .809727
- 989 Guyot, A., Protat, A., Alexander, S. P., Klekociuk, A. R., Kuma, P., & McDon-
 990 ald, A. (2022). Detection of supercooled liquid water containing clouds with
 991 ceilometers: development and evaluation of deterministic and data-driven
 992 retrievals. *Atmospheric Measurement Techniques*, 15(12), 3663–3681. doi:
 993 10.5194/amt-15-3663-2022
- 994 Harris, C. R., Millman, K. J., van der Walt, S. J., Gommers, R., Virtanen, P., Cour-
 995 napeau, D., ... Oliphant, T. E. (2020, September). Array programming with
 996 NumPy. *Nature*, 585(7825), 357–362. doi: 10.1038/s41586-020-2649-2
- 997 Hohenegger, C., Korn, P., Linardakis, L., Redler, R., Schnur, R., Adamidis, P., ...
 998 Stevens, B. (2023). ICON-Sapphire: simulating the components of the Earth
 999 system and their interactions at kilometer and subkilometer scales. *Geoscientific
 1000 Model Development*, 16(2), 779–811. doi: 10.5194/gmd-16-779-2023
- 1001 Hoppmann, M., Tippenhauer, S., & Heitland, T. (2023). *Continuous thermosalino-*
 1002 *graph oceanography along RV POLARSTERN cruise track PS123 [Dataset]*.
 1003 PANGAEA. Retrieved from <https://doi.org/10.1594/PANGAEA.938753>
 1004 doi: 10.1594/PANGAEA.938753
- 1005 Hoppmann, M., Tippenhauer, S., & Hellmer, H. H. (2023). *Continuous ther-*
 1006 *mosalinograph oceanography along RV POLARSTERN cruise track PS124*
 1007 *[Dataset]*. PANGAEA. Retrieved from <https://doi.org/10.1594/PANGAEA.938767> doi: 10.1594/PANGAEA.938767
- 1008 Hoskins, B. J., & Hodges, K. I. (2005). A new perspective on Southern Hemisphere
 1009 storm tracks. *Journal of Climate*, 18(20), 4108–4129. doi: 10.1175/JCLI3570
 1010 .1
- 1011 Hunter, J. D. (2007). Matplotlib: A 2D graphics environment. *Computing in Science
 1012 & Engineering*, 9(3), 90–95. doi: 10.1109/MCSE.2007.55
- 1013 Hyder, P., Edwards, J. M., Allan, R. P., Hewitt, H. T., Bracegirdle, T. J., Gregory,
 1014 J. M., ... Belcher, S. E. (2018). Critical Southern Ocean climate model biases
 1015 traced to atmospheric model cloud errors. *Nature Communications*, 9(1), 3625.
 1016 doi: 10.1038/s41467-018-05634-2
- 1017 Jokat, W., & Rohardt, G. (2013). *Continuous thermosalinograph oceanography along*
 1018 *POLARSTERN cruise track ANT-XXIX/5 [Dataset]*. PANGAEA. Retrieved
 1019 from <https://doi.org/10.1594/PANGAEA.816055> doi: 10.1594/PANGAEA
 1020 .816055
- 1021 Karlsson, J., Svensson, G., & Rodhe, H. (2008). Cloud radiative forcing of subtrop-
 1022 ical low level clouds in global models. *Climate Dynamics*, 30(7), 779–788. doi:
 1023 10.1007/s00382-007-0322-1
- 1024 Kattner, G., & Rohardt, G. (2012). *Continuous thermosalinograph oceanogra-*
 1025 *phy along POLARSTERN cruise track ANT-XXVIII/2 [Dataset]*. PAN-
 1026 GAEA. Retrieved from <https://doi.org/10.1594/PANGAEA.776596> doi:
 1027 10.1594/PANGAEA.776596
- 1028 Khairoutdinov, M. F., & Randall, D. A. (2003). Cloud resolving modeling of
 1029 the ARM summer 1997 IOP: Model formulation, results, uncertainties, and
 1030 sensitivities. *Journal of the Atmospheric Sciences*, 60(4), 607–625. doi:
 1031 10.1175/1520-0469(2003)060<607:CRMOTA>2.0.CO;2
- 1032 Klein, S. A., Zhang, Y., Zelinka, M. D., Pincus, R., Boyle, J., & Gleckler, P. J.
 1033 (2013). Are climate model simulations of clouds improving? an evaluation
 1034 using the ISCCP simulator. *Journal of Geophysical Research: Atmospheres*,
 1035 118(3), 1329–1342. doi: 10.1002/jgrd.50141
- 1036 Klekociuk, A. R., French, W. J. R., Alexander, S. P., Kuma, P., & McDonald, A. J.
 1037 (2020). The state of the atmosphere in the 2016 southern Kerguelen Axis cam-
 1038 paign region. *Deep Sea Research Part II: Topical Studies in Oceanography*,

- 1040 174. (Ecosystem drivers of food webs on the Kerguelen Axis of the Southern
 1041 Ocean) doi: 10.1016/j.dsr2.2019.02.001
- 1042 Knight, C. L., Mallet, M. D., Alexander, S. P., Fraser, A. D., Protat, A., & McFar-
 1043 quhar, G. M. (2024). Cloud properties and boundary layer stability above
 1044 Southern Ocean sea ice and coastal Antarctica. *Journal of Geophysical Re-*
 1045 *search: Atmospheres*, 129(10), e2022JD038280. doi: <https://doi.org/10.1029/2022JD038280>
- 1047 Knust, R., & Rohardt, G. (2011). *Continuous thermosalinograph oceanography along*
 1048 *POLARSTERN cruise track ANT-XXVII/3 [Dataset]*. PANGAEA. Retrieved
 1049 from <https://doi.org/10.1594/PANGAEA.760121> doi: 10.1594/PANGAEA
 1050 .760121
- 1051 Knust, R., & Rohardt, G. (2014). *Continuous thermosalinograph oceanography*
 1052 *along POLARSTERN cruise track PS82 (ANT-XXIX/9) [Dataset]*. PAN-
 1053 GAEA. Retrieved from <https://doi.org/10.1594/PANGAEA.839407> doi:
 1054 10.1594/PANGAEA.839407
- 1055 Koldunov, N., Kölling, T., Pedruzo-Bagazgoitia, X., Rackow, T., Redler, R.,
 1056 Sidorenko, D., ... Ziemen, F. A. (2023). *nextGEMS: output of the model*
 1057 *development cycle 3 simulations for ICON and IFS*. World Data Center for
 1058 Climate (WDCC) at DKRZ. doi: 10.26050/WDCC/nextGEMS_cyc3
- 1059 König-Langlo, G. (2011a). *Continuous meteorological surface measurement dur-*
 1060 *ing POLARSTERN cruise ANT-XXVII/2 [Dataset]*. PANGAEA. Retrieved
 1061 from <https://doi.org/10.1594/PANGAEA.760388> doi: 10.1594/PANGAEA
 1062 .760388
- 1063 König-Langlo, G. (2011b). *Continuous meteorological surface measurement dur-*
 1064 *ing POLARSTERN cruise ANT-XXVII/3 [Dataset]*. PANGAEA. Retrieved
 1065 from <https://doi.org/10.1594/PANGAEA.760389> doi: 10.1594/PANGAEA
 1066 .760389
- 1067 König-Langlo, G. (2011c). *Meteorological observations during POLARSTERN cruise*
 1068 *ANT-XXVII/2 [Dataset]*. PANGAEA. Retrieved from <https://doi.org/10.1594/PANGAEA.760392> doi: 10.1594/PANGAEA.760392
- 1069 König-Langlo, G. (2011d). *Meteorological observations during POLARSTERN cruise*
 1070 *ANT-XXVII/3 [Dataset]*. PANGAEA. Retrieved from <https://doi.org/10.1594/PANGAEA.760393> doi: 10.1594/PANGAEA.760393
- 1071 König-Langlo, G. (2011e). *Upper air soundings during POLARSTERN cruise ANT-*
 1072 *XXVII/2 [Dataset]*. PANGAEA. Retrieved from <https://doi.org/10.1594/PANGAEA.849045> doi: 10.1594/PANGAEA.849045
- 1073 König-Langlo, G. (2012a). *Continuous meteorological surface measurement dur-*
 1074 *ing POLARSTERN cruise ANT-XXVIII/2 [Dataset]*. PANGAEA. Retrieved
 1075 from <https://doi.org/10.1594/PANGAEA.784453> doi: 10.1594/PANGAEA
 1076 .784453
- 1077 König-Langlo, G. (2012b). *Continuous meteorological surface measurement dur-*
 1078 *ing POLARSTERN cruise ANT-XXVIII/3 [Dataset]*. PANGAEA. Retrieved
 1079 from <https://doi.org/10.1594/PANGAEA.784454> doi: 10.1594/PANGAEA
 1080 .784454
- 1081 König-Langlo, G. (2012c). *Continuous meteorological surface measurement dur-*
 1082 *ing POLARSTERN cruise ANT-XXVIII/4 [Dataset]*. PANGAEA. Retrieved
 1083 from <https://doi.org/10.1594/PANGAEA.784455> doi: 10.1594/PANGAEA
 1084 .784455
- 1085 König-Langlo, G. (2012d). *Meteorological observations during POLARSTERN cruise*
 1086 *ANT-XXVIII/2 [Dataset]*. PANGAEA. Retrieved from <https://doi.org/10.1594/PANGAEA.784458> doi: 10.1594/PANGAEA.784458
- 1087 König-Langlo, G. (2012e). *Meteorological observations during POLARSTERN cruise*
 1088 *ANT-XXVIII/3 [Dataset]*. PANGAEA. Retrieved from <https://doi.org/10.1594/PANGAEA.784459> doi: 10.1594/PANGAEA.784459
- 1089 König-Langlo, G. (2012f). *Meteorological observations during POLARSTERN cruise*

- 1095 *ANT-XXVIII/4 [Dataset]*. PANGAEA. Retrieved from <https://doi.org/10.1594/PANGAEA.784460> doi: 10.1594/PANGAEA.784460
- 1096 König-Langlo, G. (2012g). *Upper air soundings during POLARSTERN cruise ANT-XXVII/3 [Dataset]*. PANGAEA. Retrieved from <https://doi.org/10.1594/PANGAEA.849044> doi: 10.1594/PANGAEA.849044
- 1097 König-Langlo, G. (2012h). *Upper air soundings during POLARSTERN cruise ANT-XXVIII/2 [Dataset]*. PANGAEA. Retrieved from <https://doi.org/10.1594/PANGAEA.844866> doi: 10.1594/PANGAEA.844866
- 1098 König-Langlo, G. (2012i). *Upper air soundings during POLARSTERN cruise ANT-XXVIII/3 [Dataset]*. PANGAEA. Retrieved from <https://doi.org/10.1594/PANGAEA.844865> doi: 10.1594/PANGAEA.844865
- 1099 König-Langlo, G. (2012j). *Upper air soundings during POLARSTERN cruise ANT-XXVIII/4 [Dataset]*. PANGAEA. Retrieved from <https://doi.org/10.1594/PANGAEA.844859> doi: 10.1594/PANGAEA.844859
- 1100 König-Langlo, G. (2013a). *Continuous meteorological surface measurement during POLARSTERN cruise ANT-XXIX/2 [Dataset]*. PANGAEA. Retrieved from <https://doi.org/10.1594/PANGAEA.815472> doi: 10.1594/PANGAEA.815472
- 1101 König-Langlo, G. (2013b). *Continuous meteorological surface measurement during POLARSTERN cruise ANT-XXIX/3 [Dataset]*. PANGAEA. Retrieved from <https://doi.org/10.1594/PANGAEA.815473> doi: 10.1594/PANGAEA.815473
- 1102 König-Langlo, G. (2013c). *Continuous meteorological surface measurement during POLARSTERN cruise ANT-XXIX/4 [Dataset]*. PANGAEA. Retrieved from <https://doi.org/10.1594/PANGAEA.815723> doi: 10.1594/PANGAEA.815723
- 1103 König-Langlo, G. (2013d). *Continuous meteorological surface measurement during POLARSTERN cruise ANT-XXIX/5 [Dataset]*. PANGAEA. Retrieved from <https://doi.org/10.1594/PANGAEA.815474> doi: 10.1594/PANGAEA.815474
- 1104 König-Langlo, G. (2013e). *Continuous meteorological surface measurement during POLARSTERN cruise ANT-XXIX/6 [Dataset]*. PANGAEA. Retrieved from <https://doi.org/10.1594/PANGAEA.820733> doi: 10.1594/PANGAEA.820733
- 1105 König-Langlo, G. (2013f). *Meteorological observations during POLARSTERN cruise ANT-XXIX/2 [Dataset]*. PANGAEA. Retrieved from <https://doi.org/10.1594/PANGAEA.815476> doi: 10.1594/PANGAEA.815476
- 1106 König-Langlo, G. (2013g). *Meteorological observations during POLARSTERN cruise ANT-XXIX/3 [Dataset]*. PANGAEA. Retrieved from <https://doi.org/10.1594/PANGAEA.815477> doi: 10.1594/PANGAEA.815477
- 1107 König-Langlo, G. (2013h). *Meteorological observations during POLARSTERN cruise ANT-XXIX/4 [Dataset]*. PANGAEA. Retrieved from <https://doi.org/10.1594/PANGAEA.815724> doi: 10.1594/PANGAEA.815724
- 1108 König-Langlo, G. (2013i). *Meteorological observations during POLARSTERN cruise ANT-XXIX/5 [Dataset]*. PANGAEA. Retrieved from <https://doi.org/10.1594/PANGAEA.815478> doi: 10.1594/PANGAEA.815478
- 1109 König-Langlo, G. (2013j). *Meteorological observations during POLARSTERN cruise ANT-XXIX/6 (AWECS) [Dataset]*. PANGAEA. Retrieved from <https://doi.org/10.1594/PANGAEA.819610> doi: 10.1594/PANGAEA.819610
- 1110 König-Langlo, G. (2013k). *Meteorological observations during POLARSTERN cruise ANT-XXIX/7 [Dataset]*. PANGAEA. Retrieved from <https://doi.org/10.1594/PANGAEA.820843> doi: 10.1594/PANGAEA.820843
- 1111 König-Langlo, G. (2013l). *Upper air soundings during POLARSTERN cruise ANT-XXIX/2 [Dataset]*. PANGAEA. Retrieved from <https://doi.org/10.1594/PANGAEA.844856> doi: 10.1594/PANGAEA.844856

- 1150 König-Langlo, G. (2013m). *Upper air soundings during POLARSTERN cruise
ANT-XXIX/3 [Dataset]*. PANGAEA. Retrieved from <https://doi.org/10.1594/PANGAEA.844855> doi: 10.1594/PANGAEA.844855
- 1151
- 1152 König-Langlo, G. (2013n). *Upper air soundings during POLARSTERN cruise ANT-
XXIX/4 [Dataset]*. PANGAEA. Retrieved from <https://doi.org/10.1594/PANGAEA.844854> doi: 10.1594/PANGAEA.844854
- 1153
- 1154 König-Langlo, G. (2013o). *Upper air soundings during POLARSTERN cruise ANT-
XXIX/5 [Dataset]*. PANGAEA. Retrieved from <https://doi.org/10.1594/PANGAEA.844853> doi: 10.1594/PANGAEA.844853
- 1155
- 1156 König-Langlo, G. (2013p). *Upper air soundings during POLARSTERN cruise ANT-
XXIX/6 (AWECS) to the Antarctic in 2013 [Dataset]*. PANGAEA. Retrieved
1157 from <https://doi.org/10.1594/PANGAEA.842810> doi: 10.1594/PANGAEA
1158 .842810
- 1159
- 1160 König-Langlo, G. (2013q). *Upper air soundings during POLARSTERN cruise ANT-
XXIX/7 [Dataset]*. PANGAEA. Retrieved from <https://doi.org/10.1594/PANGAEA.844852> doi: 10.1594/PANGAEA.844852
- 1161
- 1162 König-Langlo, G. (2013r). *Upper air soundings during POLARSTERN cruise ANT-
XXIX/8 [Dataset]*. PANGAEA. Retrieved from <https://doi.org/10.1594/PANGAEA.844809> doi: 10.1594/PANGAEA.844809
- 1163
- 1164 König-Langlo, G. (2014a). *Ceilometer CL51 raw data measured during PO-
LARSTERN cruise ANT-XXIX/2, links to files [Dataset]*. PANGAEA.
1165 Retrieved from <https://doi.org/10.1594/PANGAEA.834526> doi:
1166 10.1594/PANGAEA.834526
- 1167
- 1168 König-Langlo, G. (2014b). *Ceilometer CL51 raw data measured during PO-
LARSTERN cruise ANT-XXIX/3, links to files [Dataset]*. PANGAEA.
1169 Retrieved from <https://doi.org/10.1594/PANGAEA.834527> doi:
1170 10.1594/PANGAEA.834527
- 1171
- 1172 König-Langlo, G. (2014c). *Ceilometer CL51 raw data measured during PO-
LARSTERN cruise ANT-XXIX/4, links to files [Dataset]*. PANGAEA.
1173 Retrieved from <https://doi.org/10.1594/PANGAEA.834528> doi:
1174 10.1594/PANGAEA.834528
- 1175
- 1176 König-Langlo, G. (2014d). *Ceilometer CL51 raw data measured during PO-
LARSTERN cruise ANT-XXIX/5, links to files [Dataset]*. PANGAEA.
1177 Retrieved from <https://doi.org/10.1594/PANGAEA.834529> doi:
1178 10.1594/PANGAEA.834529
- 1179
- 1180 König-Langlo, G. (2014e). *Ceilometer CL51 raw data measured during PO-
LARSTERN cruise ANT-XXIX/6 (AWECS), links to files [Dataset]*. PANGAEA.
1181 Retrieved from <https://doi.org/10.1594/PANGAEA.833801> doi:
1182 10.1594/PANGAEA.833801
- 1183
- 1184 König-Langlo, G. (2014f). *Ceilometer CL51 raw data measured during PO-
LARSTERN cruise ANT-XXIX/7, links to files [Dataset]*. PANGAEA.
1185 Retrieved from <https://doi.org/10.1594/PANGAEA.833802> doi:
1186 10.1594/PANGAEA.833802
- 1187
- 1188 König-Langlo, G. (2014g). *Ceilometer CL51 raw data measured during PO-
LARSTERN cruise ANT-XXIX/8, links to files [Dataset]*. PANGAEA.
1189 Retrieved from <https://doi.org/10.1594/PANGAEA.834530> doi:
1190 10.1594/PANGAEA.834530
- 1191
- 1192 König-Langlo, G. (2014h). *Ceilometer CL51 raw data measured during PO-
LARSTERN cruise ANT-XXVII/2, links to files [Dataset]*. PANGAEA.
1193 Retrieved from <https://doi.org/10.1594/PANGAEA.834511> doi: 10.1594/
1194 PANGAEA.834511
- 1195
- 1196 König-Langlo, G. (2014i). *Ceilometer CL51 raw data measured during PO-
LARSTERN cruise ANT-XXVII/3, links to files [Dataset]*. PANGAEA.
1197 Retrieved from <https://doi.org/10.1594/PANGAEA.834512> doi: 10.1594/
1198 PANGAEA.834512
- 1199
- 1200

- 1205 König-Langlo, G. (2014j). *Ceilometer CL51 raw data measured during PO-*
 1206 *LARSTERN cruise ANT-XXVIII/2, links to files [Dataset].* PANGAEA.
 1207 Retrieved from <https://doi.org/10.1594/PANGAEA.834518> doi: 10.1594/
 1208 PANGAEA.834518
- 1209 König-Langlo, G. (2014k). *Ceilometer CL51 raw data measured during PO-*
 1210 *LARSTERN cruise ANT-XXVIII/3, links to files [Dataset].* PANGAEA.
 1211 Retrieved from <https://doi.org/10.1594/PANGAEA.834519> doi: 10.1594/
 1212 PANGAEA.834519
- 1213 König-Langlo, G. (2014l). *Ceilometer CL51 raw data measured during PO-*
 1214 *LARSTERN cruise ANT-XXVIII/4, links to files [Dataset].* PANGAEA.
 1215 Retrieved from <https://doi.org/10.1594/PANGAEA.834520> doi: 10.1594/
 1216 PANGAEA.834520
- 1217 König-Langlo, G. (2014m). *Ceilometer CL51 raw data measured during PO-*
 1218 *LARSTERN cruise PS82 (ANT-XXIX/9), links to files [Dataset].* PAN-
 1219 GAEA. Retrieved from <https://doi.org/10.1594/PANGAEA.834531> doi:
 1220 10.1594/PANGAEA.834531
- 1221 König-Langlo, G. (2014n). *Continuous meteorological surface measurement dur-*
 1222 *ing POLARSTERN cruise ANT-XXIX/8 [Dataset].* PANGAEA. Retrieved
 1223 from <https://doi.org/10.1594/PANGAEA.832602> doi: 10.1594/PANGAEA
 1224 .832602
- 1225 König-Langlo, G. (2014o). *Continuous meteorological surface measurement during*
 1226 *POLARSTERN cruise PS82 (ANT-XXIX/9) [Dataset].* PANGAEA. Retrieved
 1227 from <https://doi.org/10.1594/PANGAEA.832603> doi: 10.1594/PANGAEA
 1228 .832603
- 1229 König-Langlo, G. (2014p). *Meteorological observations during POLARSTERN cruise*
 1230 *ANT-XXIX/8 [Dataset].* PANGAEA. Retrieved from <https://doi.org/10.1594/PANGAEA.832605> doi: 10.1594/PANGAEA.832605
- 1231 König-Langlo, G. (2014q). *Meteorological observations during POLARSTERN cruise*
 1232 *PS82 (ANT-XXIX/9) [Dataset].* PANGAEA. Retrieved from <https://doi.org/10.1594/PANGAEA.832606> doi: 10.1594/PANGAEA.832606
- 1233 König-Langlo, G. (2014r). *Upper air soundings during POLARSTERN cruise PS82*
 1234 *(ANT-XXIX/9) [Dataset].* PANGAEA. Retrieved from <https://doi.org/10.1594/PANGAEA.844805> doi: 10.1594/PANGAEA.844805
- 1235 König-Langlo, G. (2015a). *Ceilometer CL51 raw data measured during PO-*
 1236 *LARSTERN cruise PS89, links to files [Dataset].* PANGAEA. Re-
 1237 tried from <https://doi.org/10.1594/PANGAEA.844075> doi: 10.1594/
 1238 PANGAEA.844075
- 1239 König-Langlo, G. (2015b). *Continuous meteorological surface measurement during*
 1240 *POLARSTERN cruise PS89 (ANT-XXX/2) [Dataset].* PANGAEA. Retrieved
 1241 from <https://doi.org/10.1594/PANGAEA.849502> doi: 10.1594/PANGAEA
 1242 .849502
- 1243 König-Langlo, G. (2015c). *Meteorological observations during POLARSTERN cruise*
 1244 *PS89 (ANT-XXX/2) [Dataset].* PANGAEA. Retrieved from <https://doi.org/10.1594/PANGAEA.844571> doi: 10.1594/PANGAEA.844571
- 1245 König-Langlo, G. (2015d). *Upper air soundings during POLARSTERN cruise PS89*
 1246 *(ANT-XXX/2) [Dataset].* PANGAEA. Retrieved from <https://doi.org/10.1594/PANGAEA.844791> doi: 10.1594/PANGAEA.844791
- 1247 König-Langlo, G. (2016a). *Ceilometer CL51 raw data measured during PO-*
 1248 *LARSTERN cruise PS96, links to files [Dataset].* PANGAEA. Re-
 1249 tried from <https://doi.org/10.1594/PANGAEA.860516> doi: 10.1594/
 1250 PANGAEA.860516
- 1251 König-Langlo, G. (2016b). *Ceilometer CL51 raw data measured during PO-*
 1252 *LARSTERN cruise PS97, links to files [Dataset].* PANGAEA. Re-
 1253 tried from <https://doi.org/10.1594/PANGAEA.860517> doi: 10.1594/
 1254 PANGAEA.860517

- 1260 König-Langlo, G. (2016c). *Continuous meteorological surface measurement during POLARSTERN cruise ANT-XXIX/7 [Dataset]*. PANGAEA. Retrieved from <https://doi.org/10.1594/PANGAEA.858532> doi: 10.1594/PANGAEA.858532
- 1261
1262
1263
1264 König-Langlo, G. (2016d). *Continuous meteorological surface measurement during POLARSTERN cruise PS96 (ANT-XXXI/2 FROSN) [Dataset]*. PANGAEA. Retrieved from <https://doi.org/10.1594/PANGAEA.861441> doi: 10.1594/PANGAEA.861441
- 1265
1266
1267
1268 König-Langlo, G. (2016e). *Continuous meteorological surface measurement during POLARSTERN cruise PS97 (ANT-XXXI/3) [Dataset]*. PANGAEA. Retrieved from <https://doi.org/10.1594/PANGAEA.861442> doi: 10.1594/PANGAEA.861442
- 1269
1270
1271
1272 König-Langlo, G. (2016f). *Meteorological observations during POLARSTERN cruise PS96 (ANT-XXXI/2 FROSN) [Dataset]*. PANGAEA. Retrieved from <https://doi.org/10.1594/PANGAEA.861438> doi: 10.1594/PANGAEA.861438
- 1273
1274
1275
1276 König-Langlo, G. (2016g). *Meteorological observations during POLARSTERN cruise PS97 (ANT-XXXI/3) [Dataset]*. PANGAEA. Retrieved from <https://doi.org/10.1594/PANGAEA.861439> doi: 10.1594/PANGAEA.861439
- 1277
1278 König-Langlo, G. (2016h). *Upper air soundings during POLARSTERN cruise PS96 (ANT-XXXI/2 FROSN) [Dataset]*. PANGAEA. Retrieved from <https://doi.org/10.1594/PANGAEA.861658> doi: 10.1594/PANGAEA.861658
- 1279
1280
1281 König-Langlo, G. (2016i). *Upper air soundings during POLARSTERN cruise PS97 (ANT-XXXI/3) [Dataset]*. PANGAEA. Retrieved from <https://doi.org/10.1594/PANGAEA.861659> doi: 10.1594/PANGAEA.861659
- 1282
1283
1284 König-Langlo, G. (2017a). *Ceilometer CL51 raw data measured during POLARSTERN cruise PS103, links to files [Dataset]*. PANGAEA. Retrieved from <https://doi.org/10.1594/PANGAEA.871722> doi: 10.1594/PANGAEA.871722
- 1285
1286
1287
1288 König-Langlo, G. (2017b). *Ceilometer CL51 raw data measured during POLARSTERN cruise PS104, links to files [Dataset]*. PANGAEA. Retrieved from <https://doi.org/10.1594/PANGAEA.874154> doi: 10.1594/PANGAEA.874154
- 1289
1290
1291
1292 König-Langlo, G. (2017c). *Continuous meteorological surface measurement during POLARSTERN cruise PS103 (ANT-XXXII/2) [Dataset]*. PANGAEA. Retrieved from <https://doi.org/10.1594/PANGAEA.873016> doi: 10.1594/PANGAEA.873016
- 1293
1294
1295
1296 König-Langlo, G. (2017d). *Meteorological observations during POLARSTERN cruise PS103 (ANT-XXXII/2) [Dataset]*. PANGAEA. Retrieved from <https://doi.org/10.1594/PANGAEA.871721> doi: 10.1594/PANGAEA.871721
- 1297
1298
1299 König-Langlo, G. (2017e). *Meteorological observations during POLARSTERN cruise PS104 (ANT-XXXII/3) [Dataset]*. PANGAEA. Retrieved from <https://doi.org/10.1594/PANGAEA.874156> doi: 10.1594/PANGAEA.874156
- 1300
1301
1302 König-Langlo, G. (2017f). *Upper air soundings during POLARSTERN cruise PS103 (ANT-XXXII/2) [Dataset]*. PANGAEA. Retrieved from <https://doi.org/10.1594/PANGAEA.871788> doi: 10.1594/PANGAEA.871788
- 1303
1304
1305 König-Langlo, G. (2017g). *Upper air soundings during POLARSTERN cruise PS104 (ANT-XXXII/3) [Dataset]*. PANGAEA. Retrieved from <https://doi.org/10.1594/PANGAEA.874224> doi: 10.1594/PANGAEA.874224
- 1306
1307
1308 Konsta, D., Dufresne, J.-L., Chepfer, H., Vial, J., Koshiro, T., Kawai, H., ... Ogura, T. (2022). Low-level marine tropical clouds in six CMIP6 models are too few, too bright but also too compact and too homogeneous. *Geophysical Research Letters*, 49(11), e2021GL097593. doi: 10.1029/2021GL097593
- 1309
1310
1311
1312
1313
1314 Korn, P., Brüggemann, N., Jungclaus, J. H., Lorenz, S. J., Gutjahr, O., Haak, H., ... Marotzke, J. (2022). ICON-O: The ocean component of the ICON Earth

- 1315 system model—global simulation characteristics and local telescoping capability. *Journal of Advances in Modeling Earth Systems*, 14(10), e2021MS002952.
 1316 doi: 10.1029/2021MS002952
- 1317 Kremser, S., Harvey, M., Kuma, P., Hartery, S., Saint-Macary, A., McGregor, J., ...
 1318 Parsons, S. (2020). *Southern Ocean Cloud and Aerosol data set: a compilation of measurements from the 2018 Southern Ocean Ross Sea Marine Ecosystems and Environment voyage [Dataset]*. Zenodo. Retrieved from <https://doi.org/10.5281/zenodo.4060237> doi: 10.5281/zenodo.4060237
- 1319 Kremser, S., Harvey, M., Kuma, P., Hartery, S., Saint-Macary, A., McGregor, J., ...
 1320 Parsons, S. (2021). Southern Ocean cloud and aerosol data: a compilation of measurements from the 2018 Southern Ocean Ross Sea Marine Ecosystems and Environment voyage. *Earth System Science Data*, 13(7), 3115–3153. doi:
 1321 10.5194/essd-13-3115-2021
- 1322 Kuma, P. (2024). *rstool version 2.0.0 [Software]*. Retrieved from <https://github.com/peterkuma/rstool> (Accessed on 26 August 2024)
- 1323 Kuma, P., McDonald, A. J., Morgenstern, O., Alexander, S. P., Cassano, J. J., Garrett, S., ... Williams, J. (2020). Evaluation of Southern Ocean cloud in the HadGEM3 general circulation model and MERRA-2 reanalysis using ship-based observations. *Atmospheric Chemistry and Physics*, 20(11), 6607–6630. doi:
 1324 10.5194/acp-20-6607-2020
- 1325 Kuma, P., McDonald, A. J., Morgenstern, O., Querel, R., Silber, I., & Flynn, C. J.
 1326 (2021). Ground-based lidar processing and simulator framework for comparing models and observations (ALCF 1.0). *Geoscientific Model Development*, 14(1), 43–72. doi: 10.5194/gmd-14-43-2021
- 1327 Lamy, F., & Rohardt, G. (2017). *Continuous thermosalinograph oceanography along POLARSTERN cruise track PS97 (ANT-XXXI/3) [Dataset]*. PANGAEA. Retrieved from <https://doi.org/10.1594/PANGAEA.873147> doi: 10.1594/PANGAEA.873147
- 1328 Lemke, P., & Rohardt, G. (2013). *Continuous thermosalinograph oceanography along POLARSTERN cruise track ANT-XXIX/6 [Dataset]*. PANGAEA. Retrieved from <https://doi.org/10.1594/PANGAEA.819831> doi: 10.1594/PANGAEA.819831
- 1329 Lier, P., & Bach, M. (2008). PARASOL a microsatellite in the A-Train for Earth atmospheric observations. *Acta Astronautica*, 62(2), 257–263. doi: 10.1016/j.actaastro.2006.12.052
- 1330 Lin, S.-J. (2004). A “vertically Lagrangian” finite-volume dynamical core for global models. *Monthly Weather Review*, 132(10), 2293–2307. doi: 10.1175/1520-0493(2004)132<2293:AVLFDC>2.0.CO;2
- 1331 Loeb, N., Su, W., Doelling, D., Wong, T., Minnis, P., Thomas, S., & Miller, W.
 1332 (2018). 5.03 - Earth's top-of-atmosphere radiation budget. In S. Liang
 1333 (Ed.), *Comprehensive remote sensing* (p. 67-84). Oxford: Elsevier. doi:
 1334 <https://doi.org/10.1016/B978-0-12-409548-9.10367-7>
- 1335 Lucassen, M., & Rohardt, G. (2012). *Continuous thermosalinograph oceanography along POLARSTERN cruise track ANT-XXVIII/4 [Dataset]*. PANGAEA. Retrieved from <https://doi.org/10.1594/PANGAEA.802809> doi: 10.1594/PANGAEA.802809
- 1336 Luo, F., Ying, J., Liu, T., & Chen, D. (2023). Origins of Southern Ocean warm sea surface temperature bias in CMIP6 models. *npj Climate and Atmospheric Science*, 6(1), 127. doi: 10.1038/s41612-023-00456-6
- 1337 Mace, G. G., Zhang, Q., Vaughan, M., Marchand, R., Stephens, G., Trepte, C., &
 1338 Winker, D. (2009). A description of hydrometeor layer occurrence statistics derived from the first year of merged Cloudsat and CALIPSO data. *Journal of Geophysical Research: Atmospheres*, 114(D8). doi: 10.1029/2007JD009755
- 1339 Madec, G., & the NEMO System Team. (2023). *NEMO ocean engine reference manual*. Zenodo. Retrieved from <https://doi.org/10.5281/zenodo.8167700>

- 1370 doi: 10.5281/zenodo.8167700
- 1371 Marchand, R., Mace, G. G., Ackerman, T., & Stephens, G. (2008). Hydrom-
1372 eteor detection using Cloudsat—an Earth-orbiting 94-GHz cloud radar.
1373 *Journal of Atmospheric and Oceanic Technology*, 25(4), 519–533. doi:
1374 10.1175/2007JTECHA1006.1
- 1375 Mauritzen, T., Redler, R., Esch, M., Stevens, B., Hohenegger, C., Klocke, D., ...
1376 Schnur, R. (2022). Early development and tuning of a global coupled cloud
1377 resolving model, and its fast response to increasing CO₂. *Tellus A: Dynamic
1378 Meteorology and Oceanography*. doi: 10.16993/tellusa.54
- 1379 McDonald, A. J., Alexander, S. P., McFarquhar, G. M., Cassano, J. J., Plank, G. E.,
1380 Parsons, S., ... Schick, K. (2024). *Voyage data for the manuscript “Ship-based
1381 lidar evaluation of Southern Ocean clouds in the storm-resolving general cir-
1382 culation model ICON, and the ERA5 and MERRA-2 reanalyses” [Dataset]*.
1383 Zenodo. Retrieved from <https://doi.org/10.5281/zenodo.14422428> doi:
1384 10.5281/zenodo.14422428
- 1385 McDonald, A. J., Kuma, P., Pannell, M., Pettersson, O., Plank, G. E., Rozliaiani,
1386 M. A. H., & Whitehead, L. E. (2024). Evaluating cloud properties at Scott
1387 Base: Comparing ceilometer observations with ERA5, JRA55, and MERRA2
1388 reanalyses using an instrument simulator. *ESS Open Archive*. (Preprint) doi:
1389 10.22541/essoar.171820795.52152814/v1
- 1390 McErlich, C., McDonald, A., Renwick, J., & Schuddeboom, A. (2023). An assess-
1391 ment of Southern Hemisphere extratropical cyclones in ERA5 using WindSat.
1392 *Journal of Geophysical Research: Atmospheres*, 128(22), e2023JD038554. doi:
1393 10.1029/2023JD038554
- 1394 McErlich, C., McDonald, A., Schuddeboom, A., & Silber, I. (2021). Compar-
1395 ing satellite- and ground-based observations of cloud occurrence over high
1396 southern latitudes. *Journal of Geophysical Research: Atmospheres*, 126(6),
1397 e2020JD033607. doi: 10.1029/2020JD033607
- 1398 McFarquhar, G. M., Bretherton, C. S., Marchand, R., Protat, A., DeMott, P. J.,
1399 Alexander, S. P., ... McDonald, A. (2021). Observations of clouds, aerosols,
1400 precipitation, and surface radiation over the Southern Ocean: An overview of
1401 CAPRICORN, MARCUS, MICRE, and SOCRATES. *Bulletin of the American
1402 Meteorological Society*, 102(4), E894–E928. doi: 10.1175/BAMS-D-20-0132.1
- 1403 Medeiros, B., Nuijens, L., Antoniazzi, C., & Stevens, B. (2010). Low-latitude bound-
1404 ary layer clouds as seen by CALIPSO. *Journal of Geophysical Research: Atmo-*
1405 *spheres*, 115(D23), D23207. doi: 10.1029/2010JD014437
- 1406 Meissner, T., & Wentz, F. J. (2009). Wind-vector retrievals under rain with passive
1407 satellite microwave radiometers. *IEEE Transactions on Geoscience and Remote
1408 Sensing*, 47(9), 3065–3083. doi: 10.1109/TGRS.2009.2027012
- 1409 Met Office. (2010). Cartopy: a cartographic python library with a Matplotlib inter-
1410 face [Software] [Computer software manual]. Exeter, Devon. Retrieved from
1411 <https://scitools.org.uk/cartopy>
- 1412 Meyer, B., & Rohardt, G. (2013). *Continuous thermosalinograph oceanography along
1413 POLARSTERN cruise track ANT-XXIX/7 [Dataset]*. PANGAEA. Retrieved
1414 from <https://doi.org/10.1594/PANGAEA.823259> doi: 10.1594/PANGAEA
1415 .823259
- 1416 Meyer, B., & Rohardt, G. (2018). *Continuous thermosalinograph oceanography along
1417 POLARSTERN cruise track PS112 (ANT-XXXIII/3) [Dataset]*. PANGAEA.
1418 Retrieved from <https://doi.org/10.1594/PANGAEA.895580> doi: 10.1594/
1419 PANGAEA.895580
- 1420 Molod, A., Takacs, L., Suarez, M., & Bacmeister, J. (2015). Development of the
1421 GEOS-5 atmospheric general circulation model: evolution from MERRA
1422 to MERRA2. *Geoscientific Model Development*, 8(5), 1339–1356. doi:
1423 10.5194/gmd-8-1339-2015
- 1424 Nam, C., Bony, S., Dufresne, J.-L., & Chepfer, H. (2012). The ‘too few, too bright’

- 1425 tropical low-cloud problem in CMIP5 models. *Geophysical Research Letters*,
 1426 39(21), L21801. doi: 10.1029/2012GL053421
- 1427 Neu, U., Akperov, M. G., Bellenbaum, N., Benestad, R., Blender, R., Caballero, R.,
 1428 ... Wernli, H. (2013). IMILAST: A community effort to intercompare extra-
 1429 tropical cyclone detection and tracking algorithms. *Bulletin of the American
 1430 Meteorological Society*, 94(4), 529–547. doi: 10.1175/BAMS-D-11-00154.1
- 1431 nextGEMS authors team. (2023). *nextGEMS Cycle 3*. Retrieved from <https://easy.gems.dkrz.de/DYAMOND/NextGEMS/cycle3.html> (Accessed on 12 June
 1432 2024)
- 1433 nextGEMS authors team. (2024). *nextGEMS website*. Retrieved from <https://nextgems-h2020.eu> (Accessed on 17 June 2024)
- 1434 Niu, Q., McFarquhar, G. M., Marchand, R., Theisen, A., Cavallo, S. M., Flynn, C.,
 1435 ... Hill, T. C. J. (2024). 62°S witnesses the transition of boundary layer ma-
 1436 rine aerosol pattern over the Southern Ocean (50°S–68°S, 63°E–150°E) during
 1437 the spring and summer: Results from MARCUS (I). *Journal of Geophysical
 1438 Research: Atmospheres*, 129(9), e2023JD040396. doi: 10.1029/2023JD040396
- 1439 Pei, Z., Fiddes, S. L., French, W. J. R., Alexander, S. P., Mallet, M. D., Kuma, P.,
 1440 & McDonald, A. (2023). Assessing the cloud radiative bias at Macquarie
 1441 Island in the ACCESS-AM2 model. *Atmospheric Chemistry and Physics*,
 1442 23(23), 14691–14714. doi: 10.5194/acp-23-14691-2023
- 1443 Possner, A., Danker, J., & Gryspeerdt, E. (2022). Resolution dependence of South-
 1444 ern Ocean mixed-phase clouds in ICON. *ESS Open Archive*. (Preprint) doi:
 1445 10.1002/essoar.10511442.1
- 1446 Putman, W. M., & Suarez, M. (2011). Cloud-system resolving simulations with the
 1447 NASA Goddard Earth Observing System global atmospheric model (GEOS-5).
 1448 *Geophysical Research Letters*, 38(16), L16809. doi: 10.1029/2011GL048438
- 1449 Pérez-Alarcón, A., Coll-Hidalgo, P., Trigo, R. M., Nieto, R., & Gimeno, L. (2024).
 1450 CyTRACK: An open-source and user-friendly python toolbox for detecting
 1451 and tracking cyclones. *Environmental Modelling & Software*, 176, 106027. doi:
 1452 10.1016/j.envsoft.2024.106027
- 1453 Ramadoss, V., Pfannkuch, K., Protat, A., Huang, Y., Siems, S., & Possner, A.
 1454 (2024). An evaluation of cloud-precipitation structures in mixed-phase stra-
 1455 tocumuli over the southern ocean in kilometer-scale ICON simulations during
 1456 CAPRICORN. *Journal of Geophysical Research: Atmospheres*, 129(18),
 1457 e2022JD038251. doi: <https://doi.org/10.1029/2022JD038251>
- 1458 Rew, R., & Davis, G. (1990). NetCDF: an interface for scientific data access. *IEEE
 1459 Computer Graphics and Applications*, 10(4), 76–82. doi: 10.1109/38.56302
- 1460 Rienercker, M. M., Suarez, M. J., Todling, R., Bacmeister, J., Takacs, L., Liu,
 1461 H.-C., ... Nielsen, J. E. (2008). *The GEOS-5 data assimilation sys-
 1462 tem—documentation of versions 5.0.1, 5.1.0, and 5.2.0* (Tech. Rep.). NASA
 1463 Center for AeroSpace Information, 7115 Standard Drive, Hanover, MD 21076-
 1464 1320, USA. Retrieved from <https://gmao.gsfc.nasa.gov/pubs/docs/Rienecker369.pdf> (Technical Report Series on Global Modeling and Data
 1465 Assimilation, Volume 27)
- 1466 Rintoul, S. R. (2011). The Southern Ocean in the Earth system. In P. A. Berk-
 1467 man, M. A. Lang, D. W. H. Walton, & O. R. Young (Eds.), *Science diplomacy:
 1468 Antarctica, science, and the governance of international spaces* (pp. 175–
 1469 187). Washington, DC, USA: Smithsonian Institution Scholarly Press. doi:
 1470 10.5479/si.9781935623069.175
- 1471 Satoh, M., Matsuno, T., Tomita, H., Miura, H., Nasuno, T., & Iga, S. (2008). Non-
 1472 hydrostatic icosahedral atmospheric model (NICAM) for global cloud resolving
 1473 simulations. *Journal of Computational Physics*, 227(7), 3486–3514. doi:
 1474 10.1016/j.jcp.2007.02.006
- 1475 Satoh, M., Stevens, B., Judt, F., Khairoutdinov, M., Lin, S.-J., Putman, W. M., &
 1476 Düben, P. (2019). Global cloud-resolving models. *Current Climate Change*
- 1477

- Reports*, 5(3), 172–184. doi: 10.1007/s40641-019-00131-0

Schlindwein, V., & Rohardt, G. (2014). *Continuous thermosalinograph oceanography along POLARSTERN cruise track ANT-XXIX/8 [Dataset]*. PANGAEA. Retrieved from <https://doi.org/10.1594/PANGAEA.839406> doi: 10.1594/PANGAEA.839406

Schmithüsen, H. (2019a). *Radiosonde measurements during POLARSTERN cruise PS111 (ANT-XXXIII/2) [Dataset]*. PANGAEA. Retrieved from <https://doi.org/10.1594/PANGAEA.903862> doi: 10.1594/PANGAEA.903862

Schmithüsen, H. (2019b). *Radiosonde measurements during POLARSTERN cruise PS112 (ANT-XXXIII/3) [Dataset]*. PANGAEA. Retrieved from <https://doi.org/10.1594/PANGAEA.903863> doi: 10.1594/PANGAEA.903863

Schmithüsen, H. (2019c). *Radiosonde measurements during POLARSTERN cruise PS117 [Dataset]*. PANGAEA. Retrieved from <https://doi.org/10.1594/PANGAEA.903916> doi: 10.1594/PANGAEA.903916

Schmithüsen, H. (2019d). *Radiosonde measurements during POLARSTERN cruise PS118 [Dataset]*. PANGAEA. Retrieved from <https://doi.org/10.1594/PANGAEA.903922> doi: 10.1594/PANGAEA.903922

Schmithüsen, H. (2020a). *Meteorological observations during POLARSTERN cruise PS111 (ANT-XXXIII/2) [Dataset]*. PANGAEA. Retrieved from <https://doi.org/10.1594/PANGAEA.913625> doi: 10.1594/PANGAEA.913625

Schmithüsen, H. (2020b). *Meteorological observations during POLARSTERN cruise PS112 (ANT-XXXIII/3) [Dataset]*. PANGAEA. Retrieved from <https://doi.org/10.1594/PANGAEA.913626> doi: 10.1594/PANGAEA.913626

Schmithüsen, H. (2020c). *Meteorological observations during POLARSTERN cruise PS117 [Dataset]*. PANGAEA. Retrieved from <https://doi.org/10.1594/PANGAEA.913632> doi: 10.1594/PANGAEA.913632

Schmithüsen, H. (2020d). *Meteorological observations during POLARSTERN cruise PS118 [Dataset]*. PANGAEA. Retrieved from <https://doi.org/10.1594/PANGAEA.913633> doi: 10.1594/PANGAEA.913633

Schmithüsen, H. (2021a). *Ceilometer CL51 raw data measured during POLARSTERN cruise PS111, links to files [Dataset]*. PANGAEA. Retrieved from <https://doi.org/10.1594/PANGAEA.929484> doi: 10.1594/PANGAEA.929484

Schmithüsen, H. (2021b). *Ceilometer CL51 raw data measured during POLARSTERN cruise PS112, links to files [Dataset]*. PANGAEA. Retrieved from <https://doi.org/10.1594/PANGAEA.929488> doi: 10.1594/PANGAEA.929488

Schmithüsen, H. (2021c). *Ceilometer CL51 raw data measured during POLARSTERN cruise PS117, links to files [Dataset]*. PANGAEA. Retrieved from <https://doi.org/10.1594/PANGAEA.929505> doi: 10.1594/PANGAEA.929505

Schmithüsen, H. (2021d). *Ceilometer CL51 raw data measured during POLARSTERN cruise PS118, links to files [Dataset]*. PANGAEA. Retrieved from <https://doi.org/10.1594/PANGAEA.929510> doi: 10.1594/PANGAEA.929510

Schmithüsen, H. (2021e). *Ceilometer CL51 raw data measured during POLARSTERN cruise PS123, links to files [Dataset]*. PANGAEA. Retrieved from <https://doi.org/10.1594/PANGAEA.935273> doi: 10.1594/PANGAEA.935273

Schmithüsen, H. (2021f). *Ceilometer CL51 raw data measured during POLARSTERN cruise PS124, links to files [Dataset]*. PANGAEA. Retrieved from <https://doi.org/10.1594/PANGAEA.935274> doi: 10.1594/PANGAEA.935274

Schmithüsen, H. (2021g). *Continuous meteorological surface measurement during POLARSTERN cruise PS104 (ANT-XXXII/3) [Dataset]*. PANGAEA. Retrieved from <https://doi.org/10.1594/PANGAEA.935275> doi: 10.1594/PANGAEA.935275

- 1535 GAEA. Retrieved from <https://doi.org/10.1594/PANGAEA.929235> doi:
 1536 10.1594/PANGAEA.929235
- 1537 Schmithüsen, H. (2021h). *Continuous meteorological surface measurement
 1538 during POLARSTERN cruise PS111 (ANT-XXXIII/2) [Dataset]*. PANGAEA.
 1539 GAEA. Retrieved from <https://doi.org/10.1594/PANGAEA.929241> doi:
 1540 10.1594/PANGAEA.929241
- 1541 Schmithüsen, H. (2021i). *Continuous meteorological surface measurement dur-
 1542 ing POLARSTERN cruise PS112 (ANT-XXXIII/3) [Dataset]*. PANGAEA.
 1543 GAEA. Retrieved from <https://doi.org/10.1594/PANGAEA.929242> doi:
 1544 10.1594/PANGAEA.929242
- 1545 Schmithüsen, H. (2021j). *Continuous meteorological surface measurement during
 1546 POLARSTERN cruise PS117 [Dataset]*. PANGAEA. Retrieved from <https://doi.org/10.1594/PANGAEA.935214> doi: 10.1594/PANGAEA.935214
- 1547 Schmithüsen, H. (2021k). *Continuous meteorological surface measurement during
 1548 POLARSTERN cruise PS118 [Dataset]*. PANGAEA. Retrieved from <https://doi.org/10.1594/PANGAEA.935216> doi: 10.1594/PANGAEA.935216
- 1549 Schmithüsen, H. (2021l). *Continuous meteorological surface measurement during
 1550 POLARSTERN cruise PS123 [Dataset]*. PANGAEA. Retrieved from <https://doi.org/10.1594/PANGAEA.935226> doi: 10.1594/PANGAEA.935226
- 1551 Schmithüsen, H. (2021m). *Radiosonde measurements during POLARSTERN cruise
 1552 PS123 [Dataset]*. PANGAEA. Retrieved from <https://doi.org/10.1594/PANGAEA.935189> doi: 10.1594/PANGAEA.935189
- 1553 Schmithüsen, H. (2021n). *Radiosonde measurements during POLARSTERN cruise
 1554 PS124 [Dataset]*. PANGAEA. Retrieved from <https://doi.org/10.1594/PANGAEA.935190> doi: 10.1594/PANGAEA.935190
- 1555 Schmithüsen, H., Jens, H., & Wenzel, J. (2021). *Meteorological observations during
 1556 POLARSTERN cruise PS123 [Dataset]*. PANGAEA. Retrieved from <https://doi.org/10.1594/PANGAEA.935269> doi: 10.1594/PANGAEA.935269
- 1557 Schmithüsen, H., Rohleder, C., Otte, F., & Schröter, S. (2021). *Meteorological obser-
 1558 vations during POLARSTERN cruise PS124 [Dataset]*. PANGAEA. Retrieved
 1559 from <https://doi.org/10.1594/PANGAEA.935270> doi: 10.1594/PANGAEA
 1560 .935270
- 1561 Schröder, M., & Rohardt, G. (2017). *Continuous thermosalinograph oceanogra-
 1562 phy along POLARSTERN cruise track PS96 (ANT-XXXI/2) [Dataset]*. PANGAEA.
 1563 Retrieved from <https://doi.org/10.1594/PANGAEA.873151> doi: 10
 1564 .1594/PANGAEA.873151
- 1565 Schröder, M., & Rohardt, G. (2018). *Continuous thermosalinograph oceanography
 1566 along POLARSTERN cruise track PS111 (ANT-XXXIII/2) [Dataset]*. PANGAEA.
 1567 Retrieved from <https://doi.org/10.1594/PANGAEA.895579> doi: 10
 1568 .1594/PANGAEA.895579
- 1569 Schuddeboom, A., Varma, V., McDonald, A. J., Morgenstern, O., Harvey, M., Par-
 1570 sons, S., ... Furtado, K. (2019). Cluster-based evaluation of model compen-
 1571 sating errors: A case study of cloud radiative effect in the Southern Ocean.
 1572 *Geophysical Research Letters*, 46(6), 3446-3453. doi: 10.1029/2018GL081686
- 1573 Schuddeboom, A. J., & McDonald, A. J. (2021). The Southern Ocean radiative bias,
 1574 cloud compensating errors, and equilibrium climate sensitivity in CMIP6 mod-
 1575 els. *Journal of Geophysical Research: Atmospheres*, 126(22), e2021JD035310.
 1576 doi: 10.1029/2021JD035310
- 1577 SHIELD authors team. (2024). *SHIELD: System for High-resolution prediction
 1578 on Earth-to-Local Domains*. Retrieved from [https://www.gfdl.noaa.gov/
 1579 shield/](https://www.gfdl.noaa.gov/shield/) (Accessed on 18 June 2024)
- 1580 Skamarock, W. C., Klemp, J. B., Duda, M. G., Fowler, L. D., Park, S.-H., &
 1581 Ringler, T. D. (2012). A multiscale nonhydrostatic atmospheric model us-
 1582 ing centroidal Voronoi tessellations and C-grid staggering. *Monthly Weather
 1583 Review*, 140(9), 3090–3105. doi: 10.1175/MWR-D-11-00215.1
- 1584

- 1590 Stevens, B., Giorgetta, M., Esch, M., Mauritsen, T., Crueger, T., Rast, S., ...
 1591 Roeckner, E. (2013). Atmospheric component of the MPI-M Earth system
 1592 model: ECHAM6. *Journal of Advances in Modeling Earth Systems*, 5(2),
 1593 146–172. doi: 10.1002/jame.20015
- 1594 Stevens, B., Satoh, M., Auger, L., Biercamp, J., Bretherton, C. S., Chen, X., ...
 1595 Zhou, L. (2019). DYAMOND: the DYnamics of the Atmospheric general circu-
 1596 lation Modeled On Non-hydrostatic Domains. *Progress in Earth and Planetary
 1597 Science*, 6(1), 61. doi: 10.1186/s40645-019-0304-z
- 1598 Takasuka, D., Satoh, M., Miyakawa, T., Kodama, C., Klocke, D., Stevens, B., ...
 1599 Terai, C. R. (2024). A protocol and analysis of year-long simulations of
 1600 global storm-resolving models and beyond. *Research Square*. (Preprint) doi:
 1601 10.21203/rs.3.rs-4458164/v1
- 1602 Tange, O. (2011). GNU parallel: The command-line power tool. *The USENIX Mag-
 1603 azine*, 36(1), 42–47.
- 1604 Tiedtke, M. (1993). Representation of clouds in large-scale models. *Monthly Weather
 1605 Review*, 121(11), 3040–3061. doi: 10.1175/1520-0493(1993)121<3040:ROCILS>2
 1606 .0.CO;2
- 1607 Trenberth, K. E., & Fasullo, J. T. (2010). Simulation of present-day and twenty-
 1608 first-century energy budgets of the Southern Oceans. *Journal of Climate*,
 1609 23(2), 440–454. doi: 10.1175/2009JCLI3152.1
- 1610 Virtanen, P., Gommers, R., Oliphant, T. E., Haberland, M., Reddy, T., Cournau-
 1611 peau, D., ... and, Y. V.-B. (2020, feb). SciPy 1.0: fundamental algorithms
 1612 for scientific computing in Python. *Nature Methods*, 17(3), 261–272. doi:
 1613 10.1038/s41592-019-0686-2
- 1614 Voldoire, A., Decharme, B., Pianezze, J., Lebeaupin Brossier, C., Sevault, F.,
 1615 Seyfried, L., ... Riette, S. (2017). SURFEX v8.0 interface with OASIS3-MCT
 1616 to couple atmosphere with hydrology, ocean, waves and sea-ice models, from
 1617 coastal to global scales. *Geoscientific Model Development*, 10(11), 4207–4227.
 1618 doi: 10.5194/gmd-10-4207-2017
- 1619 Wall, C. J., Hartmann, D. L., & Ma, P.-L. (2017). Instantaneous linkages be-
 1620 tween clouds and large-scale meteorology over the Southern Ocean in obser-
 1621 vations and a climate model. *Journal of Climate*, 30(23), 9455–9474. doi:
 1622 10.1175/JCLI-D-17-0156.1
- 1623 Wang, C., Zhang, L., Lee, S.-K., Wu, L., & Mechoso, C. R. (2014). A global per-
 1624 spective on CMIP5 climate model biases. *Nature Climate Change*, 4(3), 201–
 1625 205. doi: 10.1038/nclimate2118
- 1626 Wang, Q., Danilov, S., Sidorenko, D., Timmermann, R., Wekerle, C., Wang, X.,
 1627 ... Schröter, J. (2014). The Finite Element Sea Ice-Ocean Model (FESOM)
 1628 v.1.4: formulation of an ocean general circulation model. *Geoscientific Model
 1629 Development*, 7(2), 663–693. doi: 10.5194/gmd-7-663-2014
- 1630 Weare, B. C. (2004). A comparison of AMIP II model cloud layer properties with
 1631 ISCCP D2 estimates. *Climate Dynamics*, 22(2), 281–292. doi: 10.1007/s00382
 1632 -003-0374-9
- 1633 Webb, M., Senior, C., Bony, S., & Morcrette, J.-J. (2001). Combining ERBE
 1634 and ISCCP data to assess clouds in the Hadley Centre, ECMWF and LMD
 1635 atmospheric climate models. *Climate Dynamics*, 17(12), 905–922. doi:
 1636 10.1007/s003820100157
- 1637 Weisman, M. L., Skamarock, W. C., & Klemp, J. B. (1997). The resolution de-
 1638 pendence of explicitly modeled convective systems. *Monthly Weather Review*,
 1639 125(4), 527–548. doi: 10.1175/1520-0493(1997)125<0527:TRDOEM>2.0.CO;2
- 1640 Whitehead, L. E., McDonald, A. J., & Guyot, A. (2023). Supercooled liquid water
 1641 cloud classification using lidar backscatter peak properties. *EGUspHERE*, 2023,
 1642 1–30. doi: 10.5194/egusphere-2023-1085
- 1643 Wiegner, M., & Gasteiger, J. (2015). Correction of water vapor absorption for
 1644 aerosol remote sensing with ceilometers. *Atmospheric Measurement Tech-*

- niques*, 8(9), 3971–3984. doi: 10.5194/amt-8-3971-2015

Wiegner, M., Mattis, I., Pattantyús-Ábrahám, M., Bravo-Aranda, J. A., Poltera, Y., Haefele, A., ... Pöhlitz, K. (2019). Aerosol backscatter profiles from ceilometers: validation of water vapor correction in the framework of CeilEx2015. *Atmospheric Measurement Techniques*, 12(1), 471–490. doi: 10.5194/amt-12-471-2019

Wielicki, B. A., Barkstrom, B. R., Harrison, E. F., Lee, R. B., Smith, G. L., & Cooper, J. E. (1996). Clouds and the Earth's Radiant Energy System (CERES): An Earth Observing System experiment. *Bulletin of the American Meteorological Society*, 77(5), 853–868. doi: 10.1175/1520-0477(1996)077<0853:CATERE>2.0.CO;2

Williams, R. G., Ceppi, P., Roussenov, V., Katavouta, A., & Meijers, A. J. S. (2023). The role of the Southern Ocean in the global climate response to carbon emissions. *Philosophical Transactions of the Royal Society A: Mathematical, Physical and Engineering Sciences*, 381(2249). doi: 10.1098/rsta.2022.0062

Wolf-Gladrow, D. A., & Rohardt, G. (2012). *Continuous thermosalinograph oceanography along POLARSTERN cruise track ANT-XXVIII/3 [Dataset]*. PAN-GAEA. Retrieved from <https://doi.org/10.1594/PANGAEA.780004> doi: 10.1594/PANGAEA.780004

Xia, Z., & McFarquhar, G. M. (2024). Dependence of cloud macrophysical properties and phase distributions on environmental conditions over the North Atlantic and Southern Ocean: Results from COMBLE and MARCUS. *Journal of Geophysical Research: Atmospheres*, 129(12), e2023JD039869. doi: 10.1029/2023JD039869

Zelinka, M. D., Myers, T. A., McCoy, D. T., Po-Chedley, S., Caldwell, P. M., Ceppi, P., ... Taylor, K. E. (2020). Causes of higher climate sensitivity in CMIP6 models. *Geophysical Research Letters*, 47(1), e2019GL085782. doi: 10.1029/2019GL085782

Zhang, M. H., Lin, W. Y., Klein, S. A., Bacmeister, J. T., Bony, S., Cederwall, R. T., ... Zhang, J. H. (2005). Comparing clouds and their seasonal variations in 10 atmospheric general circulation models with satellite measurements. *Journal of Geophysical Research: Atmospheres*, 110(D15), D15S02. doi: 10.1029/2004JD005021

Zhang, Q., Liu, B., Li, S., & Zhou, T. (2023). Understanding models' global sea surface temperature bias in mean state: From CMIP5 to CMIP6. *Geophysical Research Letters*, 50(4), e2022GL100888. doi: 10.1029/2022GL100888

Zhao, L., Wang, Y., Zhao, C., Dong, X., & Yung, Y. L. (2022). Compensating errors in cloud radiative and physical properties over the Southern Ocean in the CMIP6 climate models. *Advances in Atmospheric Sciences*, 39(12), 2156–2171. doi: 10.1007/s00376-022-2036-z